
Article:
Lesnic, D, Hussein, SO and Johansson, BT (2016) Inverse space-dependent force problems for the wave equation. Journal of Computational and Applied Mathematics, 306. pp. 10-39. ISSN 0377-0427

https://doi.org/10.1016/j.cam.2016.03.034

Inverse space-dependent force problem for the wave equation

D. Lesnic[1], S.O. Hussein[1] and B.T. Johansson[2]
[1]*Department of Applied Mathematics, University of Leeds, Leeds LS2 9JT, UK*
[2]*Aston University, School of Mathematics, Birmingham B4 7ET, UK*
E-mails: D.Lesnic@leeds.ac.uk, ml10soh@leeds.ac.uk, tomas.johansson@liu.se

Abstract. The determination of the displacement and the space-dependent force acting on a vibrating structure from measured final or time-average displacement observation is thoroughly investigated. Several issues related to the existence and uniqueness of solution of the linear but ill-posed inverse problems are highlighted. After that, in order to capture the solution a variational formulation is proposed and the gradient of the least-squares functional that is minimized is rigorously and explicitly derived. Numerical results obtained using the Landweber method and the conjugate gradient method are presented and discussed illustrating the convergence of the iterative procedures for exact input data. Furthermore, for noisy data the semi-convergence phenomenon appears, as expected, and stability is restored by stopping the iterations according to the discrepancy principle criterion once the residual becomes close to the amount of noise. The present investigation will be significant to researchers concerned with wave propagation and control of vibrating structures.

Keywords: Inverse force problem; Finite difference method; Landweber method; Conjugate gradient method; Wave equation.

1 Introduction

We consider the problem of force identification from measured data for the hyperbolic wave equation. This inverse formulation is significant to modelling several practical applications related to unknown force loads and control. Because part of the cause of the physical phenomenon is unknown one has to compensate for this lack of information by measuring an appropriate part of the effect. What quantity to measure is the delicate choice/constraint when formulating inverse problems, but a proper formulation would be able to ensure that the unknown force can be uniquely retrieved from the proposed additional measurements.

Prior to this study, the reconstruction of a space-dependent force in the wave equation from Cauchy data measurements of both displacement and its normal derivative on the boundary has been attempted in [3, 10, 11]. This inverse formulation is, as expected, improperly posed because the unknown output force $f(x)$ depends on x in the domain Ω, whilst the known input data, say u and $\partial_n u$, depend on (x,t) on the boundary $\partial\Omega \times (0,T)$. Although the uniqueness of solution still holds, [6, 14, 18], it seems more natural to measure instead information about the displacement $u(x,t)$ for $x \in \Omega$ and time $t = T$, or the time-averaged displacement $\int_0^T u(x,t)dt$ for $x \in \Omega$. This way, the output-input mapping satisfies the meta-theorem that the overposed data and the unknown force function lie in the same direction, [15]. This spacewise-dependent force $f(x)$ identification from the upper-base spacewise dependent displacement measurement $u(x,T)$ has been investigated theoretically in Section 8.2 of [16], where the uniqueness of solution was proved. For other wave related force identification studies which use the final time displacement data we refer to [9] which

employs a weak solution approach for a quite general inverse problem with a highly non-unique solution, and to [17] which nicely introduces a quasi-nonlinearity in the governing wave equation to resolve the non-uniqueness of solution. The other inverse problem generated by the measurement of the time-averaged displacement $\int_0^T u(x,t)dt$ which we investigate in our study is new. Essentially, the same inverse problem with unknown spacewise dependent right-hand side source in the governing equation arises also for the parabolic heat equation in the thermal field, see [8, 13].

The plan of the paper is as follows. Section 2 introduces the inverse problem formulations, whilst Sections 3 and 4 highlight several issues related to the existence, uniqueness and stability of solution of the direct and inverse problems, respectively. Section 5 presents the variational formulations of the inverse problems under investigation and derives explicitly the expressions for the gradients of the least-squares functionals which are minimized. Section 6 describes the iterative Landweber method accommodated and applied in order to obtain regularized stable solutions, whilst Section 7 illustrates and discusses extensive numerical results in both one and two dimensions, for the recovery of both smooth and non-smooth force functions. Furthermore, the conjugate gradient method (CGM) is also described and employed for one of the examples. A numerical extension to two-dimensions is presented in Section 8 and finally, conclusions are presented in Section 9.

2 Problem formulation

Assume that we have a medium, denoted by Ω, occupying a bounded sufficiently smooth domain in $\mathbb{R}^n$, where $n \geq 1$. The boundary of Ω is denoted by $\partial\Omega$, and we define the space-time cylinder $Q_T = \Omega \times (0,T)$, where $T > 0$. We wish to find the displacement $u(x,t)$ and the force $f(x)$ in the hyperbolic wave equation

$$u_{tt} - \mathcal{L}u = f(x)g(x,t) + \chi(x,t) =: F(x,t) \quad \text{in} \quad Q_T, \tag{1}$$

where g and χ are given functions, and, in general, for a homogeneous medium we have $\mathcal{L} = \nabla^2$ the Laplacian operator. For inhomogeneous media, we can have $\mathcal{L}u = c^2(x)\nabla^2 u$, or $\nabla.(K(x)\nabla u)$, where K and c are given positive material properties, [4].

Equation (1) has to be solved subject to prescribed initial conditions

$$u(x,0) = \varphi(x) \quad x \in \Omega, \tag{2}$$

$$u_t(x,0) = \psi(x) \quad x \in \Omega, \tag{3}$$

prescribed homogenous Dirichlet boundary conditions,

$$u(x,t) = 0, \quad (x,t) \in \partial\Omega \times (0,T), \tag{4}$$

and the additional final displacement measurement

$$u(x,T) = u_T(x), \quad x \in \Omega, \tag{5}$$

or, the time-average displacement measurement

$$\int_0^T \omega(t)u(x,t)dt = U_T(x), \quad x \in \Omega, \tag{6}$$

where ω is a given weight function. One can also have the additional final speed measurement $u_t(x,T) = v_T(x)$ for $x \in \Omega$, see [9], but we do not investigate in detail this case herein because it is similar to the displacement specification (5).

3 Direct problem

Well-posedness of the direct problem (1)-(4) when f is given, is provided in Section 7 of [2] for example. Suitable space are: $F \in L^2(Q_T)$, $\varphi \in H_0^1(\Omega)$ with $\mathcal{L}\varphi \in L^2(\Omega)$, and $\psi \in H_0^1(\Omega)$, then $u \in C^2(0,T;L^2(\Omega))$ with $u(t) \in H_0^1(\Omega)$ and $\mathcal{L}u(t) \in L^2(\Omega)$ for $t \in [0,T]$.

One can also study weak solutions $u \in L^2(0,T;H_0^1(\Omega))$ with $u_t \in L^2(0,T;L^2(\Omega))$ and $u_{tt} \in L^2(0,T;H^{-1}(\Omega))$. Such a weak solution exists and is unique provided that $\varphi \in H_0^1(\Omega)$, $\psi \in L^2(\Omega)$ and $F \in L^2(Q_T)$. Note that, as usual, this implies $u \in C([0,T];L^2(\Omega))$ and $u_t \in C([0,T];H^{-1}(\Omega))$, which, in particular, yield that the restrictions at $t = 0$ of the solution and its derivative make sense. Moreover, we have the estimate

$$\begin{aligned}&\max_{0\le t\le T}\left(||u(.,t)||_{H_0^1(\Omega)} + ||u_t(.,t)||_{L^2(\Omega)}\right) + ||u_{tt}||_{L^2(0,T;H^{-1}(\Omega))}\\ &\le C\left(||F||_{L^2(0,T;L^2(\Omega))} + ||\varphi||_{H_0^1(\Omega)} + ||\psi||_{L^2(\Omega)}\right),\end{aligned} \tag{7}$$

for some positive constant C.

Similar considerations can be done for the formally adjoint backward hyperbolic problem to (1)-(4),

$$v_{tt} - \mathcal{L}^* v = G(x,t), \quad (x,t) \in Q_T, \tag{8}$$

$$v(x,T) = \zeta(x), \quad v_t(x,T) = \xi(x), \quad x \in \Omega, \tag{9}$$

$$v(x,t) = 0, \quad (x,t) \in \partial\Omega \times (0,T), \tag{10}$$

where $\mathcal{L}^*$ is the adjoint of $\mathcal{L}$.

Furthermore, we have, using integration by parts, the following Green-type formula:

$$\begin{aligned}&\int_\Omega (u_t(x,T)\zeta(x) - \psi(x)v(x,0))dx - \int_\Omega (u(x,T)\xi(x) - \varphi(x)v_t(x,0))dx\\ &\quad = \int_0^T \int_\Omega F(x,t)v(x,t)dxdt - \int_0^T \int_\Omega G(x,t)u(x,t)dxdt.\end{aligned} \tag{11}$$

3.1 Abstract setting formulation

It is possible to formulate the direct problem (1)-(4) in a more general abstract setting, as described in Chapter 8 of [16], by considering the problem

$$u'' = \mathcal{L}u(t) + F(t), \quad t \in [0,T], \tag{12}$$

$$u(0) = \varphi, \quad u'(0) = \psi, \tag{13}$$

where $\mathcal{L}$ is a closed linear operator with a dense domain of definition $D(\mathcal{L})$ on a Hilbert space X. We assume that $\mathcal{L}$ generates a strongly continuous cosine function $C(t) = \cos(\sqrt{-\mathcal{L}}t)$, such that equation (12) is hyperbolic. In the case of a self-adjoint operator, the previous assumption is equivalent to say that $\mathcal{L}$ is semi-bounded from above, [16, p.525]. According to [16, p.538], if

$$\varphi \in D(\mathcal{L}) := \{u \in X | C(t)u \in C^2(\mathbb{R})\}, \tag{14}$$

$$\psi \in E := \{u \in X | C(t)u \in C^1(\mathbb{R})\}, \tag{15}$$

$$F \in C^1([0,T];X) \oplus C([0,T];D(\mathcal{L})), \tag{16}$$

then the direct problem (12) and (13) has a unique solution in the class of functions

$$u \in C^2([0,T];X) \cap C([0,T];D(\mathcal{L})). \tag{17}$$

Furthermore, one can represent explicitly this solution as

$$u(t) = C(t)\varphi + S(t)\psi + \int_0^t S(t-s)F(s)ds, \tag{18}$$

where $S(t) = \int_0^t C(s)ds = \frac{1}{\sqrt{-\mathcal{L}}}\sin(\sqrt{-\mathcal{L}}t)$ is the associated sine function.

4 Inverse problem

Consider first, for simplicity, the one-dimensional case, i.e. $n = 1$, and take $\Omega = (0, L)$, where $L > 0$ represents the length of a vibrating string. Let us also take $\chi(x,t) = 0$, $g(x,t) = 1$ and $\mathcal{L} = \partial^2/\partial x^2$. Then, in [3] it was remarked that the inverse force problem (1)-(5) has a unique solution if and only if $T/L \notin \mathbb{Q}$, i.e. T/L is an irrational number. This follows immediately from the separation of variables, whereas for $\varphi = \psi = 0$ and $g = 1$ the solution of the inverse problem

$$u_{tt} - u_{xx} = f(x), \quad (x,t) \in (0,L) \times (0,T), \tag{19}$$

$$u(x,0) = u_t(x,0) = 0, \quad x \in (0,L), \tag{20}$$

$$u(0,t) = u(L,t) = 0, \quad t \in (0,T), \tag{21}$$

$$u(x,T) = 0, \quad x \in (0,L), \tag{22}$$

is given by

$$u(x,t) = \frac{\sqrt{2}}{\pi^2}\sum_{k=1}^{\infty}\frac{c_k}{k^2}\left(1 - \cos\left(\frac{k\pi t}{L}\right)\right)\sin\left(\frac{k\pi x}{L}\right), \tag{23}$$

$$f(x) = \sum_{k=1}^{\infty} c_k \sin\left(\frac{k\pi x}{L}\right), \tag{24}$$

where

$$c_k = \frac{\sqrt{2}}{L}\int_0^L f(x)\sin\left(\frac{k\pi x}{L}\right)dx, \quad k \geq 1. \tag{25}$$

Now, in order to impose (22) we apply (23) at $t = T$ to obtain

$$0 = \frac{\sqrt{2}}{\pi^2} \sum_{k=1}^{\infty} \frac{c_k}{k^2} \left(1 - \cos\left(\frac{k\pi T}{L}\right)\right) \sin\left(\frac{k\pi x}{L}\right), \quad x \in (0, L). \tag{26}$$

One can easily observe that $c_k = 0$ for all $k \geq 1$, and hence from (23) and (24), $u = f = 0$, if and only if $T/L \notin \mathbb{Q}$. Moreover, this condition cannot be removed even if one additionally prescribe $u_t(x, T)$, as it can be easily seen by differentiating (23) with respect to t. However, if we consider the additional time-average displacement measurement (6) (with say $\omega = 1$) instead of (5), by integrating (23) with respect to t and make it zero, we obtain

$$0 = \frac{\sqrt{2}}{\pi^2} \sum_{k=1}^{\infty} \frac{c_k}{k^2} \left(T - \frac{L}{k\pi} \sin\left(\frac{k\pi T}{L}\right)\right) \sin\left(\frac{k\pi x}{L}\right), \quad x \in (0, L). \tag{27}$$

Since $\frac{k\pi T}{L} > \sin\left(\frac{k\pi T}{L}\right)$ for all $k \in \mathbb{N}^*$, we then obtain that $c_k = 0$ for all $k \in \mathbb{N}^*$ and hence, from (23) and (24), that $u = f = 0$. Thus, the inverse problem (19)-(21) together with the integral condition

$$\int_0^T u(x, t)dt = 0, \quad x \in (0, L), \tag{28}$$

has only the trivial solution, which in turn implies that the solution of the inverse problem given by equations (19)-(21) and the time-average displacement measurement

$$\int_0^T u(x, t)dt = U_T(x), \quad x \in (0, L), \tag{29}$$

is unique, with no restriction on the ratio T/L being irrational number or not. Of course, in the case of an arbitrary integrable weight function $\omega(t)$ in (6), the necessary and sufficient condition for uniqueness becomes

$$\int_0^T \omega(t) \left(1 - \cos\left(\frac{k\pi t}{L}\right)\right) dt \neq 0, \quad \forall\ k \in \mathbb{N}^*. \tag{30}$$

4.1 Abstract setting formulation of inverse problems

Returning to the abstract setting of subsection 3.1 and viz. Section 2, we consider the inverse problem of determining the displacement u and the force f satisfying

$$u'' = \mathcal{L}u(t) + g(t)f, \quad t \in [0, T], \tag{31}$$

subject to the initial conditions (13) and the additional measurement

$$u(T) = u_T \tag{32}$$

or

$$\int_0^T \omega(t)u(t)dt = U_T. \tag{33}$$

First, the following theorem gives the unique solvability of the inverse problem (13), (31) and (32).

Theorem 1.
In the abstract settings of subsection 3.1, let $\mathcal{L}$ be a self-adjoint and semi-bounded from above operator in the Hilbert space X and assume that the input data is admissible, i.e.

$$\varphi \in D(\mathcal{L}),\ \psi \in E,\ g \in C^1([0,T];X),\ \chi \in C^1([0,T];X) \oplus C([0,T];D(\mathcal{L})), \tag{34}$$

and

$$u_T \in D(\mathcal{L}). \tag{35}$$

Then the inverse problem (13), (31) *and* (32) *has a unique solution $u \in C^2([0,T];X) \cap C([0,T];D(\mathcal{L}))$, $f \in X$ if, see Corollary 8.2.7 of [16], g is non-negative and strictly increasing, as a function of $t \in [0,T]$, or if, see Corollary 8.2.8 of [16], $g \equiv 1$ and $1 \notin \overline{Z}$, where*

$$Z := \{\cos(\sqrt{-\lambda}\ T) \mid \lambda \in \Sigma(\mathcal{L})\backslash\{0\}\}, \tag{36}$$

and $\Sigma(\mathcal{L})$ denotes the spectrum of the operator $\mathcal{L}$.

In the above, the value $g(s)$ is identified with the operator of multiplication by the number $g(s)$ in the space X.

Remark that in the previous one-dimensional setting of the inverse problem (19)-(22) the condition that $1 \notin \overline{Z}$ recasts as $1-\cos(\sqrt{-\lambda}\ T) \neq 0$, where $\lambda = -n^2\pi^2/L^2$ for $n \in \mathbb{N}^*$, which is equivalent to say that $T/L \notin \mathbb{Q}$.

We note that for $\mathcal{L} = \nabla^2$, $\Omega \in C^1$, $\varphi,\ \psi,\ u_T \in C^1(\Omega)$ satisfying compatibility conditions and $g \in C^1(Q_T)$ satisfying $g(x,t) > 0$, $g_t(x,t) > 0$, $\forall (x,t) \in \overline{Q}_T$, the existence of solution, i.e. the solvability of the inverse problem (1)-(5) was also established in [1] in the classes of functions $f \in L^2(\Omega)$, $u \in L^2(0,T;H^1(\Omega))$, $u_{tt} \in L^2(Q_T)$ and $\nabla^2 u \in L^2(Q_T)$.

Second, for the inverse problem (13), (31) and (33) we also have the existence and uniqueness of solution as given by the following theorem.

Theorem 2.
In the abstract setting of Theorem 1 and with the same input admissible data (34), *and*

$$\omega = 1, \quad U_T \in D(\mathcal{L}), \tag{37}$$

the inverse problem (13), (31) *and* (33) *has a unique solution $u \in C^2([0,T];X) \cap C([0,T];D(\mathcal{L}))$, $f \in X$, if $0 \not\equiv g$ is non-negative, as a function of $t \in [0,T]$.*

Proof. On applying (6) to (18) results in

$$\Phi(\mathcal{L})f = U_T - S(T)\varphi - \frac{(1-C(T))}{-\mathcal{L}}\psi - \int_0^T \int_0^t S(t-s)\chi(s)dsdt, \tag{38}$$

where

$$\Phi(\mathcal{L}) = \int_0^T \int_0^t g(s)S(t-s)dsdt = \int_0^T \int_0^t g(s)\frac{\sin(\sqrt{-\mathcal{L}}(t-s))}{\sqrt{-\mathcal{L}}}dsdt. \tag{39}$$

Since $\mathcal{L}$ is self-adjoint operator, it is semi-bounded from above and hence it is representable as $\mathcal{L} = \int_{-\infty}^{b} \lambda dE_\lambda$, where b is some real number and E_λ is the spectral resolution of unity of the operator $\mathcal{L}$, see [16, p.502]. This has the property that every $h \in X$ can be put in correspondence with the measure on the real linear through the relation $d\mu_h(\lambda) = d < E_\lambda h, h >_H$. This suggests that for the expression (39) we define the function $\Phi : \mathbb{R} \to \mathbb{R}$ as

$$\Phi(\lambda) = \begin{cases} \frac{1}{\sqrt{-\lambda}} \int_0^T \int_0^t g(s) \sin(\sqrt{-\lambda}(t-s)) ds dt, & \text{if} \quad \lambda < 0 \\ \int_0^T \int_0^t g(s)(t-s) ds dt, & \text{if} \quad \lambda = 0 \\ \frac{1}{\sqrt{\lambda}} \int_0^T \int_0^t g(s) \sinh(\sqrt{\lambda}(t-s)) ds dt, & \text{if} \quad \lambda > 0. \end{cases} \tag{40}$$

We can also extend this function by analytical continuation to be an entire function on the whole complex plane $\lambda \in \mathbb{C}$. Since $\mathcal{L}$ is self-adjoint it follows that $\Sigma(\mathcal{L}) \subset \mathbb{R}$ and we first show that the function Φ defined by (39) has no zero on the real line. Clearly, since $0 \not\equiv g \in C^1([0,T])$ is non-negative, $\Phi(\lambda) > 0$ for $\lambda \geq 0$. Consider now

$$\Phi(\lambda) = \frac{1}{\sqrt{-\lambda}} \int_0^T \int_0^t g(s) \sin(\sqrt{-\lambda}(t-s)) ds dt, \quad \text{for} \quad \lambda < 0. \tag{41}$$

Using the change of variables $s \longmapsto t - s$ and denoting $\sqrt{-\lambda} = \mu$ we show that

$$\int_0^T \int_0^t g(t-s) \sin(\mu s) ds dt > 0, \quad \text{for} \quad \mu > 0. \tag{42}$$

Proceeding as in [16, p.512-513], if $\mu \leq \pi/T$ then $\mu s \leq \pi$ for $0 \leq s \leq t \leq T$ and thus $\sin(\mu s) \geq 0$ and the inequality (42) follows immediately. If $\mu > \pi/T$ then let $N \in \mathbb{N}^*$ be the positive integer such that $2\pi N/\mu$ is the nearest to T from the right. Defining $\tilde{g} : [0,T] \to \mathbb{R}$ by $\tilde{g}(t) = \int_0^t g(t-s) \sin(\mu s) ds, \ t \in [0,T]$, it is easy to remark that $\tilde{g}(t - \pi/\mu) + \tilde{g}(t) = \int_0^{\pi/\mu} g(t-s) \sin(\mu s) ds \geq 0$, for $t \in [\pi/\mu, T]$. Extending the function $\tilde{g}$ to be zero on the interval $[T, 2\pi N/\mu]$, the integral in (42) recasts as

$$\begin{aligned} &\int_0^T \int_0^t g(t-s) \sin(\mu s) ds dt = \int_0^T \tilde{g}(t) dt = \sum_{k=1}^{N} \int_{2\pi(k-1)/\mu}^{2\pi k/\mu} \tilde{g}(t) dt \\ &= \sum_{k=1}^{N} \left(\int_{2\pi(k-1)/\mu}^{\pi(2k-1)/\mu} \tilde{g}(t) dt + \int_{\pi(2k-1)/\mu}^{2k\pi/\mu} \tilde{g}(t) dt \right) = \sum_{k=1}^{N} \int_{\pi(2k-1)/\mu}^{2k\pi/\mu} (\tilde{g}(t - \pi/\mu) + \tilde{g}(t)) dt \\ &= \sum_{k=1}^{N} \int_{(2k-1)\pi/\mu}^{2k\pi/\mu} \int_0^{\pi/\mu} g(t-s) \sin(\mu s) ds dt > 0, \end{aligned}$$

where the last inequality holds strictly because $0 \not\equiv g(t) \geq 0$ and $g \in C^1[0,T]$.

This concludes that the function Φ defined by (41) has no zeros on the real line (in fact it is strictly positive for $\lambda \in \mathbb{R}$). In particular, it implies that the solution of the inverse problem is unique.

Integrating by parts in (41) and making the substitution $t - s$ for s, we obtain

$$\begin{aligned} \Phi(\lambda) &= -\frac{1}{\lambda} \int_0^T \left(g(t) - g(0) \cos(\sqrt{-\lambda} t) - \int_0^t g'(t-s) \cos(\sqrt{-\lambda} s) ds \right) dt \\ &= -\frac{1}{\lambda} \left(\int_0^T g(t) dt - \frac{g(0) \sin(\sqrt{-\lambda} T)}{\sqrt{-\lambda}} - \int_0^T \int_0^t g'(t-s) \cos(\sqrt{-\lambda} s) ds dt \right), \ \lambda \in (-\infty, 0). \end{aligned}$$

Since $g \in C^1[0,T]$ it follows that

$$\Phi(\lambda) = -\frac{1}{\lambda}\int_0^T g(t)dt + O\left(\frac{1}{|\lambda|}\right), \text{ as } \lambda \to -\infty.$$

Thus $\Phi(\lambda) \geq -\frac{c}{\lambda}$, as $\lambda \to -\infty$, where $c = \int_0^T g(t)dt > 0$. Finally, this inequality together with the fact that the right hand-side of (38) is in $D(\mathcal{L})$ imply the existence of a solution $u \in C^2([0,T];X) \cap C([0,T];D(\mathcal{L}))$, $f \in X$, see [16, p.553 and Th.8.2.2].

Remark. In the particular case $\chi = 0$, $g = 1$ remark that (38) simplifies as

$$\left(\frac{T - S(T)}{-\mathcal{L}}\right) f = U_T - S(T)\varphi - \frac{(1 - C(T))}{-\mathcal{L}}\psi$$

which, since $T > S(T)$, it yields the solution for the force explicitly being given by

$$f = \frac{-\mathcal{L}U_T + S(T)\mathcal{L}\varphi - (1 - C(T))\psi}{T - S(T)}. \tag{43}$$

The solution for the displacement is also given explicitly by (18) which, for $\chi = 0$, $g = 1$, simplifies as

$$\begin{aligned} u(t) &= C(t)\varphi + S(t)\psi + \left(\frac{1 - C(t)}{-\mathcal{L}}\right) f \\ &= C(t)\varphi + S(t)\psi + \left(\frac{1 - C(t)}{T - S(T)}\right)\left(U_T - S(T)\varphi - \frac{(1 - C(t))}{-\mathcal{L}}\psi\right). \end{aligned} \tag{44}$$

Even if one has proved that the solution exists and is unique, both inverse problems (1)-(5) and (1)-(4), (6) are still ill-posed since the continuous dependence upon the input data (5) or (6) is violated. This can easily be seen from the following example of instability.

Example of instability
Let $\Omega = (0, L = \pi)$ and, for $n \in \mathbb{N}^*$ take

$$u_n(x,t) = \frac{(1 - \cos(nt))\sin(nx)}{n^{3/2}}, \quad (x,t) \in (0,\pi) \times (0,T)$$

which satisfies the wave equation with homogenous initial and Dirichlet boundary conditions,

$$u_{nT}(x) = u_n(x,T) = \frac{(1 - \cos(nT))\sin(nx)}{n^{3/2}}, \quad x \in (0,\pi)$$

$$U_{nT}(x) = \int_0^T u_n(x,t)dt = \frac{\sin(nx)}{n^{3/2}}\left(T - \frac{\sin(nT)}{n}\right), \quad x \in (0,\pi)$$

and the force

$$f_n(x) = n^{1/2}\sin(nx), \quad x \in (0,\pi).$$

One can observe that whilst all the input data tends to zero, the force $f_n(x)$ becomes oscillatory and unbounded, as $n \to \infty$.

5 Variational formulation of the inverse problem

For the solution of the inverse problem (1)-(5), define the operator $A : L^2(\Omega) \to L^2(\Omega)$ by

$$Af = u_f(\cdot, T), \tag{45}$$

where $u_f(x,t)$ is the unique weak solution of the direct problem (1)-(4) corresponding to the given force f. The operator A is bounded and affine. By A_0 we denote the similar linear operator defined for $\varphi = \psi = 0$. The inverse problem (1)-(5) recasts as

$$Af = u_T. \tag{46}$$

Since in practice u_T is contaminated with random noisy errors it is convenient to minimize the least-squares cost functional $J : L^2(\Omega) \to \mathbb{R}_+$ defined by

$$J(f) = \frac{1}{2}||Af - u_T||^2_{L^2(\Omega)}. \tag{47}$$

It can be shown that J is weakly continuous on closed and convex subsets of $L^2(\Omega)$, which in turn, due to Weierstrass' theorem implies that there exists a solution to the minimization of (47), [9]. In what follows we will show that J is Frechet differentiable and derive its gradient. For this, let u_h solve (1)-(4) with $f = h \in L^2(\Omega)$ and $\varphi = \psi = 0$. Moreover, let u_f solve (1)-(4). Then,

$$\begin{aligned} &J(f+h) - J(f) = \frac{1}{2}||Af + A_0h - u_T||^2_{L^2(\Omega)} - \frac{1}{2}||Af - u_T||^2_{L^2(\Omega)} \\ &= \int_\Omega (Af(x) - u_T(x))A_0h(x)dx + \frac{1}{2}\int_\Omega (A_0h(x))^2 dx. \end{aligned} \tag{48}$$

The first term in the right-hand side can, using the definition of the operator A_0, be rewritten as

$$\int_\Omega (Af(x) - u_T(x))A_0h(x)dx = \int_\Omega (u_f(x,T) - u_T(x))\, u_h(x,T)dx. \tag{49}$$

Let v_1 be the solution to the adjoint problem (8)-(10) with $\zeta = G = 0$ and $\xi = Af - u_T = u_f(.,T) - u_T$. From Green's formula (11) applied to v_1 and u_h it then follows that

$$\begin{aligned} &\int_\Omega (u_f(x,T) - u_T(x))u_h(x,T)dx = -\int_0^T \int_\Omega h(x)g(x,t)v_1(x,t)dxdt \\ &= -\int_\Omega h(x)\left(\int_0^T g(x,t)v_1(x,t)dt\right)dx. \end{aligned} \tag{50}$$

From (48) and (50), and since $||A_0h||^2_{L^2(\Omega)}$ can be estimated by $||h||^2_{L^2(\Omega)}$ due to (7), see also [9] for one-dimensional explicit estimates, it follows that the functional J is Frechet differentiable and its gradient is given by

$$J'(f) = -\int_0^T g(x,t)v_1(x,t)dt, \tag{51}$$

where v_1 solves

$$(v_1)_{tt} - \mathcal{L}^* v_1 = 0, \quad (x,t) \in Q_T, \tag{52}$$

$$v_1(x,T)=0, \quad (v_1)_t(x,T)=u_f(x,T)-u_T(x), \quad x\in\Omega, \tag{53}$$

$$v_1(x,t)=0, \quad (x,t)\in\partial\Omega\times(0,T). \tag{54}$$

One can show that J is in fact twice Frechet differentiable and convex. For this, let v_2 be the solution of the adjoint problem (8)-(10) with $\zeta=G=0$ and $\xi=u_h(\cdot,T)$. From Green's formula (11) applied to the functions u_h and v_2 we obtain

$$-\int_\Omega u_h^2(x,T)dx=\int_0^T\int_\Omega h(x)g(x,t)v_2(x,t)dxdt. \tag{55}$$

Following a similar argument as above we can obtain that

$$J''(f)h=-\int_0^T g(x,t)v_2(x,t)dt. \tag{56}$$

Then from (55) and (56), we obtain that

$$(J''(f)h,h)_{L^2(\Omega)}=||u_h(.,T)||^2_{L^2(\Omega)}\geq 0, \tag{57}$$

which implies that J is convex.

Similarly, for the solution of the inverse problem (1)-(4), (6), we define the operator $\tilde{A}:L^2(\Omega)\to L^2(\Omega)$ by

$$\tilde{A}f=\int_0^T\omega(t)u_f(.,t)dt, \tag{58}$$

which is bounded and affine and by $\tilde{A}_0$ denote its linear part. Then the inverse problem (1)-(4), (6) recasts as

$$\tilde{A}f=U_T. \tag{59}$$

As in the previous case, since the right-hand side is contaminated with noise, we seek a quasi-solution to (59) in the form of minimizing the cost functional $\tilde{J}:L^2(\Omega)\to\mathbb{R}_+$ defined by

$$\tilde{J}(f):=\frac{1}{2}||\tilde{A}f-U_T||^2_{L^2(\Omega)}. \tag{60}$$

As in (48) and (50), we obtain that

$$\tilde{J}(f+h)-\tilde{J}(f)=\frac{1}{2}\int_\Omega(\tilde{A}_0h(x))^2dx+\int_\Omega\left(\int_0^T\omega(t)u_h(x,t)dt\right)$$
$$\times\left(\int_0^T\omega(t)u_f(x,t)dt-U_T(x)\right)dx. \tag{61}$$

We discuss first the particular case when the weight function $\omega(t)$ is a non-zero constant, say equal to unity, and then the general case.

(i) In the particular case when $\omega(t)\equiv 1$, i.e. (6) recasts as

$$\int_0^T u(x,t)dt=U_T(x), \quad x\in\Omega, \tag{62}$$

expression (61) becomes

$$\tilde{J}(f+h)-\tilde{J}(f)=\frac{1}{2}\int_\Omega(\tilde{A}_0h(x))^2dx+\int_\Omega\left(\int_0^T u_h(x,t)dt\right)\left(\int_0^T u_f(x,t)dt-U_T(x)\right)dx. \tag{63}$$

Let $\tilde{v}_1$ be the solution of the adjoint problem (8)-(10) with $\zeta=G=0$ and $\xi=\tilde{A}f-U_T=\int_0^T u_f(.,t)dt-U_T$. It is then straightforward to observe that the function

$$w_h(x,t):=\int_0^t u_h(x,s)ds, \tag{64}$$

satisfies the wave equation with homogenous initial and boundary conditions and right-hand side equal to $\left(\int_0^T g(x,s)ds\right)h(x)$. Then, from Green's formula (11) applied to w_h and $\tilde{v}_1$ it follows from (63) that

$$\tilde{J}(f+\delta)-\tilde{J}(f)=\frac{1}{2}\int_\Omega(\tilde{A}_0h(x))^2dx-\int_\Omega\int_0^T h(x)\int_0^t g(x,s)ds\ \tilde{v}_1(x,t)dtdx. \tag{65}$$

From this it follows that

$$\tilde{J}'(f)=-\int_0^T\left(\int_0^t g(x,s)ds\right)\tilde{v}_1(x,t)dt. \tag{66}$$

(ii) In the general case, we rewrite (61) as

$$\begin{aligned}\tilde{J}(f+\delta)-\tilde{J}(f)&=\frac{1}{2}\int_\Omega(\tilde{A}h(x))^2dx\\&+\int_\Omega\int_0^T\omega(t)u_h(x,t)\left(\int_0^T\omega(\tau)u_f(x,\tau)d\tau-U_T(x)\right)dtdx.\end{aligned} \tag{67}$$

Let $\tilde{V}_1$ be the solution of the adjoint problem (8)-(10) with $\xi=\zeta=0$ and $G(x,t)=\omega(t)\left(\int_0^T\omega(\tau)u_f(x,\tau)d\tau-U_T\right)$. Then, Green's formula (11) applied to $\tilde{V}_1$ and u_h implies that the last term in (67) is equal to

$$\int_0^T\int_\Omega h(x)g(x,t)\tilde{V}_1(x,t)dxdt,$$

and consequently,

$$\tilde{J}'(f)=\int_0^T g(x,t)\tilde{V}_1(x,t)dt. \tag{68}$$

Let us finally show that (68) reduces to (66) when $\omega(t)\equiv 1$. In such a situation, the problems for $\tilde{v}_1$ and $\tilde{V}_1$ are given by

$$\begin{cases}\tilde{v}_{1tt}-\mathcal{L}^*\tilde{v}_{1xx}=0,\\ \tilde{v}_1(x,T)=0,\quad \tilde{v}_{1t}(x,T)=\int_0^T u_f(x,t)dt-U_T(x),\quad x\in\Omega,\\ \tilde{v}_1(x,t)=0,\quad (x,t)\in\partial\Omega\times(0,T),\end{cases}$$

$$\begin{cases}\tilde{V}_{1tt}-\mathcal{L}^*\tilde{V}_{1xx}=\int_0^T u_f(x,t)dt-U_T(x),\\ \tilde{V}_1(x,T)=0,\quad \tilde{V}_{1t}(x,T)=0,\quad x\in\Omega\\ \tilde{V}_1(x,t)=0,\quad (x,t)\in\partial\Omega\times(0,T).\end{cases}$$

One can observe that $\tilde{V}_{1t}(x,t) = \tilde{v}_1(x,t)$. Then, starting from (68) we derive, using integration by parts, that

$$\tilde{J}'(f) = \int_0^T g(x,t)\tilde{V}_1(x,t)dt = \left(\int_0^T g(x,s)ds\right)\tilde{V}_1(x,t)\Big|_{t=0}^{t=T}$$
$$-\int_0^T \left(\int_0^t g(x,s)ds\right)\tilde{V}_{1t}(x,t)dt = -\int_0^T \left(\int_0^t g(x,s)ds\right)\tilde{v}_1(x,t)dt. \tag{69}$$

Hence, (66) and (68) coincide in the case $\omega(t) \equiv 1$.

6 An iterative procedure for the inverse problem

Once the gradient of the functional J (or $\tilde{J}$) has been explicitly derived, as described in the previous section, we can apply the iterative Landweber method, see e.g. [7], for obtaining a stable solution to the inverse problem, as follows:

(i) Choose an arbitrary function $f_0 \in L^2(\Omega)$. Let u_0 be the solution of the direct problem (1)-(4) with $f = f_0$.

(ii) Assume that f_k and u_k have been constructed. For the inverse problem (1)-(5), let v_k solve the adjoint problem (8)-(10) with $\zeta = G = 0$ and

$$\xi_k(x) = u_k(x,T) - u_T(x), \quad x \in \Omega, \tag{70}$$

and calculate the gradient (51) given by

$$z_k(x) = -\int_0^T g(x,t)v_k(x,t)dt, \quad x \in \Omega. \tag{71}$$

For the inverse problem (1)-(4) and (62) let $\tilde{v}_k$ solve the adjoint problem (8)-(10) with $\zeta = G = 0$ and

$$\xi_k(x) = \int_0^T u_k(x,t)dt - U_T(x), \quad x \in \Omega, \tag{72}$$

and calculate the gradient (66) given by

$$z_k(x) = -\int_0^T \left(\int_0^t g(x,s)ds\right)\tilde{v}_k(x,t)dt, \quad x \in \Omega. \tag{73}$$

(iii) Construct the new iterate for the force given by

$$f_{k+1}(x) = f_k(x) - \gamma z_k(x), \quad x \in \Omega, \tag{74}$$

where $0 < \gamma < \frac{2}{||A||^2}$ (respectively $\frac{2}{||\tilde{A}||^2}$) is a relaxation factor to be prescribed and the spectral norm of the operator A (respectively $\tilde{A}$) is defined as

$$||A|| = \sup_{f \in L^2(\Omega)\setminus\{0\}} \frac{||Af||_{L^2(\Omega)}}{||f||_{L^2(\Omega)}}. \tag{75}$$

Let u_{k+1} be the solution of the direct problem (1)-(4) with $f = f_{k+1}$.

(iv) Repeat steps (ii) and (iii) until convergence is achieved in the case of exact data u_T (or U_T). In the case of noisy data

$$||u_T - u_T^\epsilon||_{L^2(\Omega)} \leq \epsilon, \quad \text{or} \quad ||U_T - U_T^\epsilon||_{L^2(\Omega)} \leq \epsilon \tag{76}$$

we can use the Morozov discrepancy principle, see e.g. [5,7], to terminate the iterations. This suggests choosing the stopping index $k = k(\epsilon)$ as the smallest k for which

$$||u_k^\epsilon(.,T) - u_T^\epsilon||_{L^2(\Omega)} \leq \tau\epsilon, \quad \text{or} \quad \left\| \int_0^T \omega(t) u_k^\epsilon(.,t) - U_T^\epsilon \right\|_{L^2(\Omega)} \leq \tau\epsilon, \tag{77}$$

where $\tau > 1$ is some constant to be prescribed. According to (47) and (60), criterion (77) can be rewritten as

$$J(f_k) \leq \tau^2 \frac{\epsilon^2}{2}, \quad \text{or} \quad \tilde{J}(f_k) \leq \tau^2 \frac{\epsilon^2}{2}. \tag{78}$$

7 Numerical results and discussion

In all examples in this section we take, for simplicity, $\omega = T = 1$, $\chi = 0$ and $\mathcal{L} = \nabla^2$ the Laplacian operator. The first five examples are one-dimensional, i.e. $n = 1$ and $\Omega = (0, L)$ with $L = 1$ for simplicity, whilst the sixth example shows the extension of the analysis to higher dimensions, e.g. $n = 2$-dimensions. We take the initial guess arbitrary such as $f_0 \equiv 0$. Also, except for Example 5, where we investigate the influence of the relaxation parameter γ on the speed of convergence, in all other examples we take $\gamma = 1$.

7.1 Example 1

Consider first the direct problem (1)-(4) given by wave equation

$$u_{tt} - u_{xx} = f(x)g(x,t), \quad (x,t) \in (0,1) \times (0,1), \tag{79}$$

and the input data

$$u(x,0) = \varphi(x) = 2\sin(\pi x), \quad u_t(x,0) = \psi(x) = 0, \quad x \in [0,1], \tag{80}$$

$$u(0,t) = u(1,t) = 0, \quad t \in (0,1], \tag{81}$$

$$g(x,t) = 1, \quad (x,t) \in (0,1) \times (0,1). \tag{82}$$

$$f(x) = \pi^2 \sin(\pi x), \quad x \in (0,1). \tag{83}$$

The exact solution of this problem is given by

$$u(x,t) = \sin(\pi x)(\cos(\pi t) + 1), \quad (x,t) \in [0,1] \times [0,1]. \tag{84}$$

We will illustrate the numerical results for obtaining the final displacement

$$u(x,T) = u(x,1) = u_T(x) = 0, \quad x \in [0,1], \tag{85}$$

and the time-average displacement

$$\int_0^T u(x,t)dt = \int_0^1 u(x,t)dt = U_T(x) = \sin(\pi x), \quad x \in [0,1], \tag{86}$$

as this will become the input data in the inverse problem later on. The discrete finite-difference form of the problem (79)-(81) is as follows. We divide the solution domain $(0,L)\times(0,T)$ into M and N subintervals of equal space length Δx and time-step Δt, where $\Delta x = L/M$ and $\Delta t = T/N$. We denote $u_{i,j} := u(x_i,t_j)$, where $x_i = i\Delta x$, $t_j = j\Delta t$, and $f_i := f(x_i)$, and $g_{i,j} := g(x_i,t_j)$ for $i = \overline{0,M}$, $j = \overline{0,N}$. Then, a central-difference approximation to equations (79)-(81) at the mesh points $(x_i,t_j) = (i\Delta x, j\Delta t)$ of the rectangular mesh covering the solution domain $(0,L)\times(0,T)$ is,

$$u_{i,j+1} = r^2u_{i+1,j} + 2(1-r^2)u_{i,j} + r^2u_{i-1,j} - u_{i,j-1} + (\Delta t)^2 f_i g_{i,j}, \quad i = \overline{1,(M-1)}, \quad j = \overline{1,(N-1)}, \tag{87}$$

$$u_{i,0} = \varphi(x_i), \quad i = \overline{0,M}, \quad \frac{u_{i,1}-u_{i,-1}}{2\Delta t} = \psi(x_i), \quad i = \overline{1,(M-1)}, \tag{88}$$

$$u_{0,j} = 0, \quad u_{M,j} = 0, \quad j = \overline{1,N}, \tag{89}$$

where $r = \Delta t/\Delta x$. Equation (87) represents an explicit FDM which is stable if $r \le 1$, giving approximate values for the solution at mesh points along $t = 2\Delta t, 3\Delta t, ...$, as soon as the solution at the mesh points along $t = \Delta t$ has been determined. Putting $j = 0$ in equation (87) and using (88), we obtain

$$u_{i,1} = \frac{1}{2}r^2\varphi(x_{i+1}) + (1-r^2)\varphi(x_i) + \frac{1}{2}r^2\varphi(x_{i-1}) + (\Delta t)\psi(x_i) + \frac{1}{2}(\Delta t)^2 f_i g_{i,0}, \quad i = \overline{1,(M-1)}. \tag{90}$$

For finding the numerical solution to (85), we put $j = N-1$ in (87). And for (86) we use the trapezoidal rule approximation

$$\int_0^T u(x_i,t)dt = \frac{\Delta t}{2}\left(\varphi(x_i) + 2\sum_{j=1}^{N-1} u(x_i,t_j) + u(x_i,t_N)\right), \quad i = \overline{1,M-1}. \tag{91}$$

The absolute errors between the exact solution (85) and the numerical solution for u_T, and also between (86) and (91) for U_T, are shown in Figure 1. From this figure it can be seen that the numerical solutions for u_T and U_T converge to the exact solutions (85) and (86), respectively, as the FDM mesh size decreases. We consider next solving the inverse problem with fixed $N = M = 80$ and $\gamma = 1$.

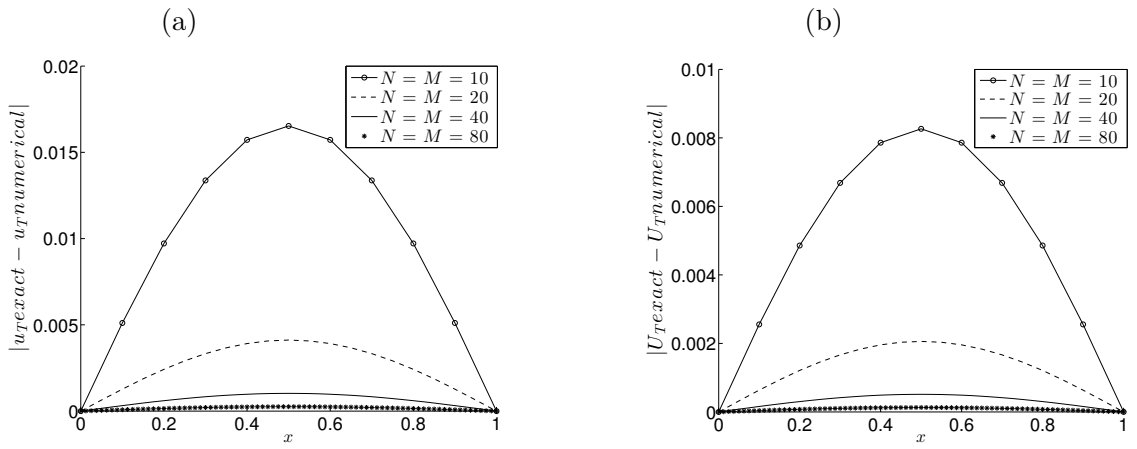

Figure 1: The absolute errors between exact and numerical solutions for (a) $u_T(x)$ and (b) $U_T(x)$, for $N = M \in \{10, 20, 40, 80\}$ for the direct problem of Example 1.

7.1.1 Inverse problem

Since from (82) we have $g \equiv 1$, and also since $T/L = 1 \in \mathbb{Q}$ we do not have the uniqueness of solution of the inverse problem (79)-(81) when measuring the final displacement (85). Therefore, for Example 1 we only consider the inverse problem (79)-(81) with the time-average displacement measurement (86) which, according to the discussion in subsection 4, has a unique solution given by equations (83) and (84).

The objective function (60) given by

$$\tilde{J}(f_k) = \frac{1}{2}||\xi_k||^2 = \frac{1}{2}\sum_{i=1}^{M-1} \xi_k^2(x_i), \tag{92}$$

where ξ_k is given by (72), is plotted in Figure 2(a), as a function of the number of iterations k. From this figure it can be seen that convergence of $\tilde{J}$ is achieved after about 300 iterations. Figure 2(b) shows the error between the exact solution f and numerical solution f_k defined by

$$E(f_k) = ||f_{exact} - f_k|| = \sqrt{\sum_{i=1}^{M-1} (f(x_i) - f_k(x_i))^2}, \tag{93}$$

as a function of the number of iterations. From this figure it can be seen a monotonic decreasing convergence to zero of the error (93).

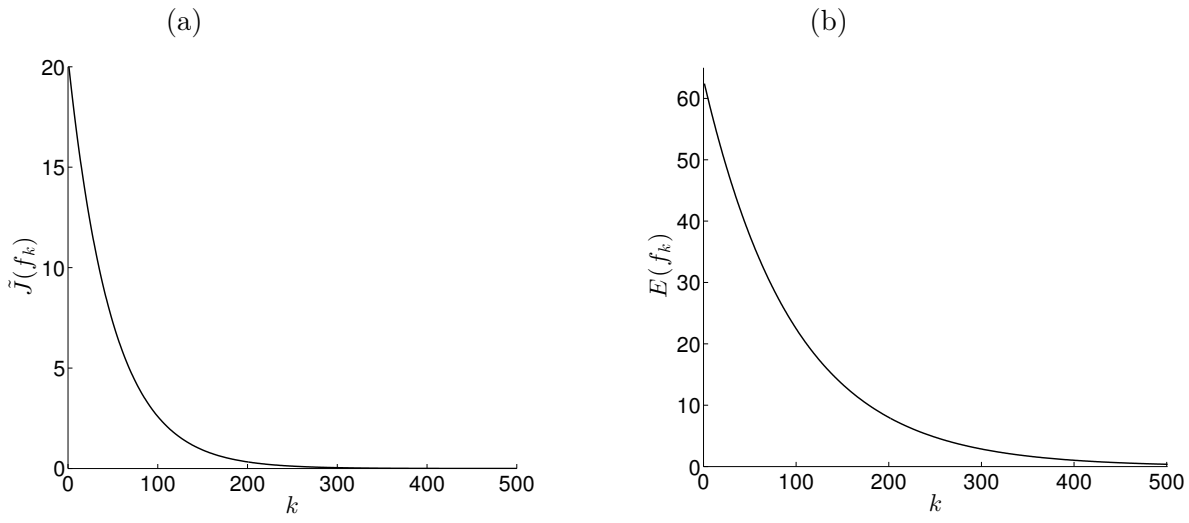

Figure 2: (a) The objective function $\tilde{J}(f_k)$ and (b) the accuracy error $E(f_k)$, versus the number of iterations $k = \overline{1, 500}$, no noise for the inverse problem of Example 1.

Figure 3 shows the numerical solution f_k at various iteration numbers k. From this figure a monotonic increasing convergence of the numerical solution f_k towards the exact solution (83) can be clearly observed.

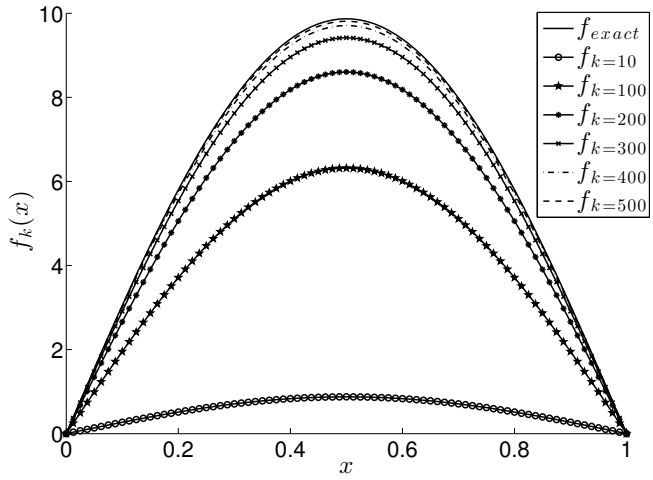

Figure 3: The numerical solution f_k at various iteration numbers k, in comparison with the exact solution (83), no noise for the inverse problem of Example 1.

In practice, the additional observation (6) comes from measurement which is inherently contaminated with errors. We therefore model this by replacing the exact data U_T by the noisy data

$$U_T^{\epsilon}(x_i) = U_T(x_i) + \epsilon_i, \quad i = \overline{1, (M-1)}, \tag{94}$$

where $(\epsilon_i)_{i=\overline{1,M-1}}$ are random noisy variables generated (using the MATLAB routine 'normrd') from a Gaussian normal distribution with mean zero and standard deviation $\sigma = p \times \max_{x\in[0,L]} |U_T(x)|$, where p represents the percentage of noise. The total amount of noise

introduced in the objective functional (60) is then given by

$$\frac{1}{2}\epsilon^2 = \frac{1}{2}\sum_{i=1}^{M-1}\epsilon_i^2. \tag{95}$$

In order to investigate the stability of the numerical solution we include some $p \in \{10, 30, 50\}\%$ noise into the input data (86), as given by equation (94). The objective functional $\tilde{J}(f_k)$ and the errors $E(f_k)$ are shown in Figure 4 for $k = \overline{1, 500}$ iterations. In Figure 4(a) the threshold $\tau^2\frac{\epsilon^2}{2}$ (with $\tau = 1.15$) in the stopping criterion (78) is included by horizontal line. Intersecting the horizontal line $y = \tau^2\frac{\epsilon^2}{2}$ with the graph of the objective functional $\tilde{J}(f_k)$ yields the stopping iteration number k_{discr} given by the discrepancy principle criterion (78). On the other hand, the minimum of the curve $E(f_k)$ in Figure 4(b) yields the optimal iteration number k_{opt}. For various percentages of noise p, the values of k_{discr} and k_{opt} together with the corresponding accuracy errors (93) are given in Table 1 for better illustrative purposes. From Figures 4(a), 4(b) and Table 1 it can be seen that there is not much difference between k_{opt} and k_{discr} for all percentages of noise p considered and this adds to the robustness of the numerical iterative method employed.

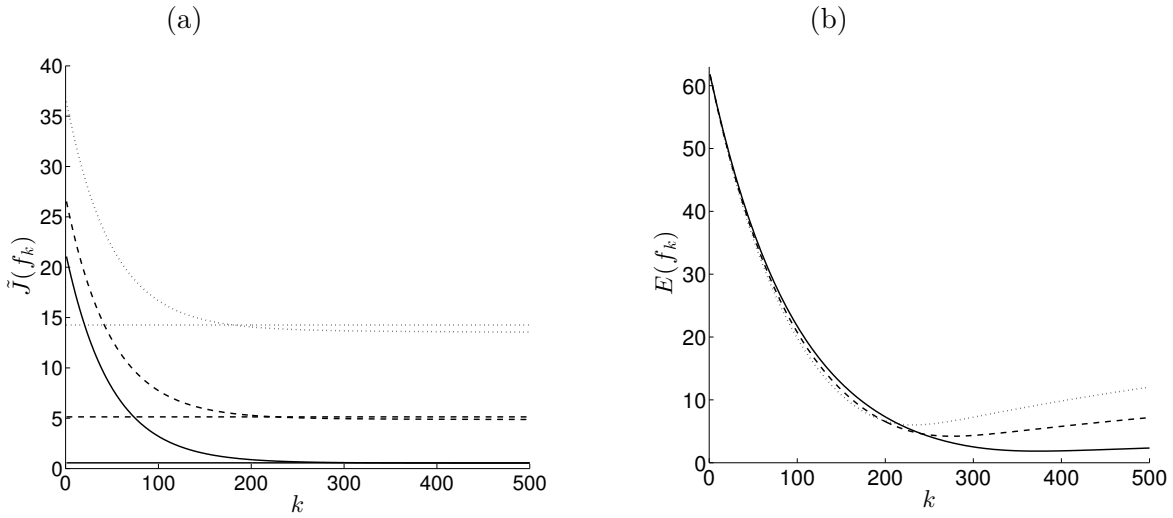

Figure 4: (a) The objective function $\tilde{J}(f_k)$ and (b) the accuracy error $E(f_k)$, versus the number of iterations $k = \overline{1, 500}$, for $p = 10\%$ (—), $p = 30\%$ (- - -) and $p = 50\%$ ($\cdots$) noise for the inverse problem of Example 1. The horizontal lines in (a) represent the threshold $\tau^2\epsilon^2/2$ with $\tau = 1.15$.

Table 1: The stopping iteration number k_{discr} chosen according to the discrepancy principle criterion (78) (with $\tau = 1.15$), as illustrated in Figure 4(a), and the optimal iteration number k_{opt} chosen according to the minimum of the accuracy error function (93) in Figure 4(b) for various percentages of noise $p \in \{10, 30, 50\}\%$ for Example 1. The corresponding accuracy errors $E(f_{k_{discr}})$ and $E(f_{k_{opt}})$ are also included.

p	10%	30%	50%
k_{opt}	373	276	232
$E(f_{k_{opt}})$	1.8471	4.2181	6.0124
k_{discr}	300	245	205
$E(f_{k_{discr}})$	2.5213	4.5269	6.4347

Figures 5(a) and 5(b) show the regularized numerical solution for $f(x)$ obtained with various values of the iteration numbers listed in Table 1, namely, $k_{opt} \in \{373, 276, 232\}$ and $k_{discr} \in \{240, 225, 220\}$, respectively, for $p \in \{10, 30, 50\}\%$ noisy data. From these figures it can be seen that there is not much difference obtained between the corresponding curves in Figures 5(a) and 5(b), except perhaps slightly for $p = 10\%$. Moreover, the numerical results illustrated in Figure 5(b) reveal that stable numerical solutions are obtained if one stops the iteration process according to the discrepancy principle (78). Stability is further maintained even for large percentages of noise such as $p = 50\%$. Furthermore, as expected, numerical results in Figure 5(b) become more accurate as the percentage of noise p decreases.

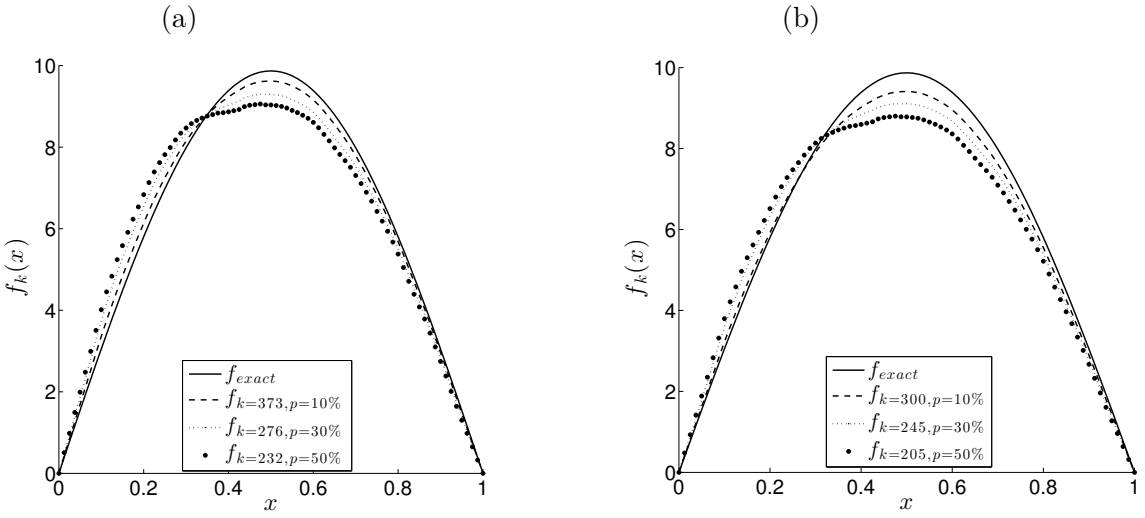

Figure 5: The exact solution f in comparison with the numerical solution f_k for (a) $k_{opt} \in \{373, 276, 232\}$ and (b) $k_{discr} \in \{300, 245, 205\}$, for $p \in \{10, 30, 50\}\%$ noise, for the inverse problem of Example 1.

7.2 Example 2

Consider the inverse problem given by the wave equation (79) with the input data (81),

$$u(x, 0) = \varphi(x) = \sin(\pi x), \quad u_t(x, 0) = \psi(x) = \sin(\pi x), \quad x \in [0, 1], \tag{96}$$

$$g(x, t) = e^t(\pi^2 + 1), \quad (x, t) \in (0, 1) \times (0, 1), \tag{97}$$

and the diplacement measurement at the final time $t = T = 1$

$$u(x,t) = u(x,1) = u_T(x) = \sin(\pi x)e, \quad x \in [0,1], \tag{98}$$

or, and the time-average displacement

$$\int_0^T u(x,t)dt = \int_0^1 u(x,t)dt = U_T(x) = \sin(\pi x)(e-1), \quad x \in [0,1]. \tag{99}$$

One can easily observe that the function (97) satisfies $g(x,t) \geq 0, g_t(x,t) > 0, \forall (x,t) \in \overline{Q}_T$ and hence, according to Theorems 1 and 2, both the inverse problems (79), (81), (96), (98), and (79), (81), (96), (99) have unique solutions. In fact, it can readily be checked by direct substitution that the analytical solution of both problems is given by

$$u(x,t) \;\; = \;\; \sin(\pi x)e^t, \quad (x,t) \in [0,1] \times [0,1], \tag{100}$$

$$f(x) = \sin(\pi x), \quad x \in (0,1). \tag{101}$$

In the numerical simulations we fix $N = M = 80$ and $\gamma = 1$.

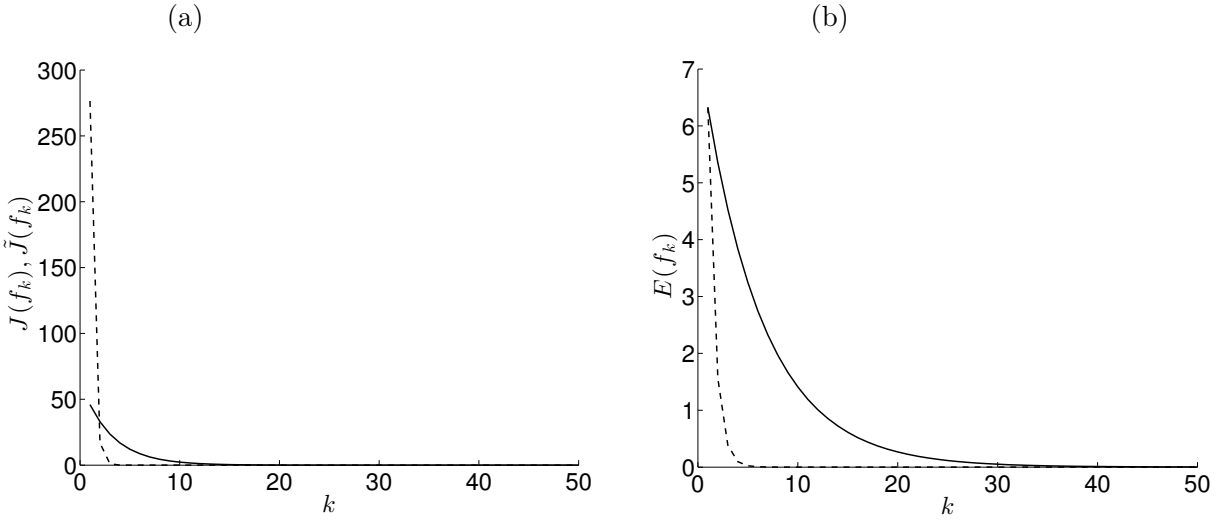

Figure 6: (a) The objective functions $J(f_k)$, $\tilde{J}(f_k)$ and (b) the accuracy error $E(f_k)$, versus the number of iterations $k = \overline{1,50}$, no noise for the inverse problem of Example 2 with the displacement measurement (98) (- - -) and with the time-average displacement measurement (99) (—).

For exact data, i.e. no noise in (98) and (99), Figures 6 and 7 are analogous to Figures 2 and 3 of Example 1 and similar conclusions can be drawn, except that now, for Example 2 with the time-average displacement measurement (99), the convergence is about 10 times faster than for Example 1. Furthermore, by inspecting Figures 6 and 7 it can be seen that for Example 2 the convergence is 5 times faster when using the displacement measurement (98) than when using the time-average displacement measurement (99).

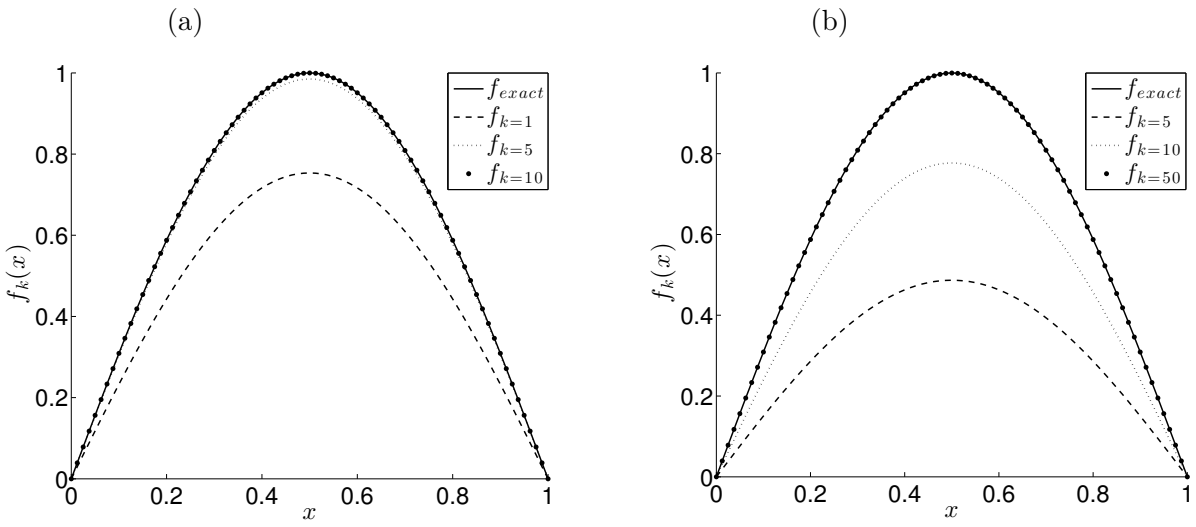

Figure 7: The numerical solution f_k at various iteration numbers k, in comparison with the exact solution (101), no noise for the inverse problem of Example 2 with (a) the displacement measurement (98), and (b) the time-average displacement measurement (99).

In order to investigate the stability of the numerical solutions we include some $p \in \{1, 3, 5\}\%$ noise into the input data (98) (or (99)), as given by a similar expression to (94). For this noisy data, Figures 8, 9 and Table 2 are analogous to Figures 4, 5 and Table 1 of Example 1 and similar conclusions can be drawn. Stability is achieved if the iterations are stopped at the index k_{discr} which is much closer to k_{opt} for Example 2 than for Example 1 because the amount of noise is much smaller (10 times) in the former case. For the same reason, the agreement between the numerical and analytical solution is much better in Figure 9 than in Figure 5. The constant $\tau > 1$ giving the threshold $\tau^2\epsilon^2/2$ seems also important and, for some interesting discussion on its choice, we refer to [5].

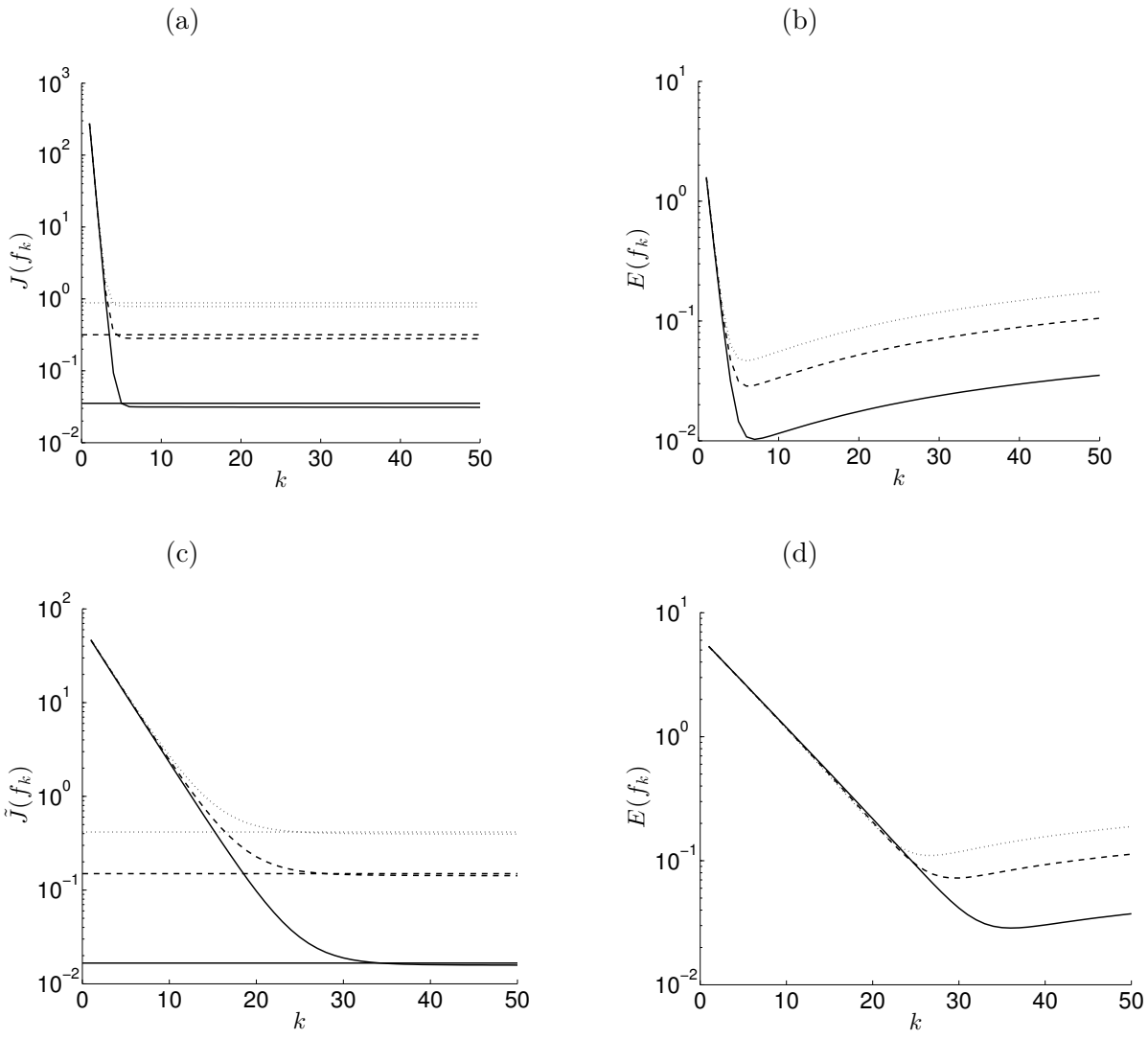

Figure 8: (a) The objective function $J(f_k)$ and (b) the corresponding accuracy error $E(f_k)$ for the inverse problem of Example 2 with the displacement measurement (98), and (c) the objective function $\tilde{J}(f_k)$ and (d) the corresponding accuracy error $E(f_k)$ for the inverse problem of Example 2 with the time-average displace measurement (99). All curves are as functions of the number of iterations $k = \overline{1, 50}$, for $p = 1\%$ (—), $p = 3\%$ (- - -) and $p = 5\%$ ($\cdots$) noise. The horizontal lines in (a) and (c) represent the threshold $\tau^2\epsilon^2/2$ with $\tau = 1.15$ and $\tau = 1.25$, respectively.

Table 2: The stopping iteration number k_{discr} chosen according to the discrepancy principle criterion (78), as illustrated in Figures 8(a) and 8(c), and the optimal iteration number k_{opt} chosen according to the minimum of the accuracy error function (93) in Figures 8(b) and 8(d), for various percentages of noise $p \in \{1, 3, 5\}\%$ for Example 2 with the displacement measurement (98) and $\tau = 1.15$ (upper part of the table) and with the time-average displacement measurement (99) and $\tau = 1.25$ (lower part of the table). The corresponding accuracy errors $E(f_{k_{discr}})$ and $E(f_{k_{opt}})$ are also included.

p	1%	3%	5%
k_{opt}	7	6	6
$E(f_{k_{opt}})$	0.0102	0.0286	0.0464
k_{discr}	6	5	4
$E(f_{k_{discr}})$	0.0107	0.0313	0.0632
k_{opt}	36	30	27
$E(f_{k_{opt}})$	0.0286	0.0725	0.1102
k_{discr}	33	27	24
$E(f_{k_{discr}})$	0.0310	0.0778	0.1200

So far, we have tested successfully examples for which analytical solutions for the displacement and force are available, as given by equations (83) and (84) for Example 1, and (100) and (101) for Example 2. The next three examples that we test concern quite arbitrary input data for which an analytical solution for the displacement $u(x, t)$ is not readily available.

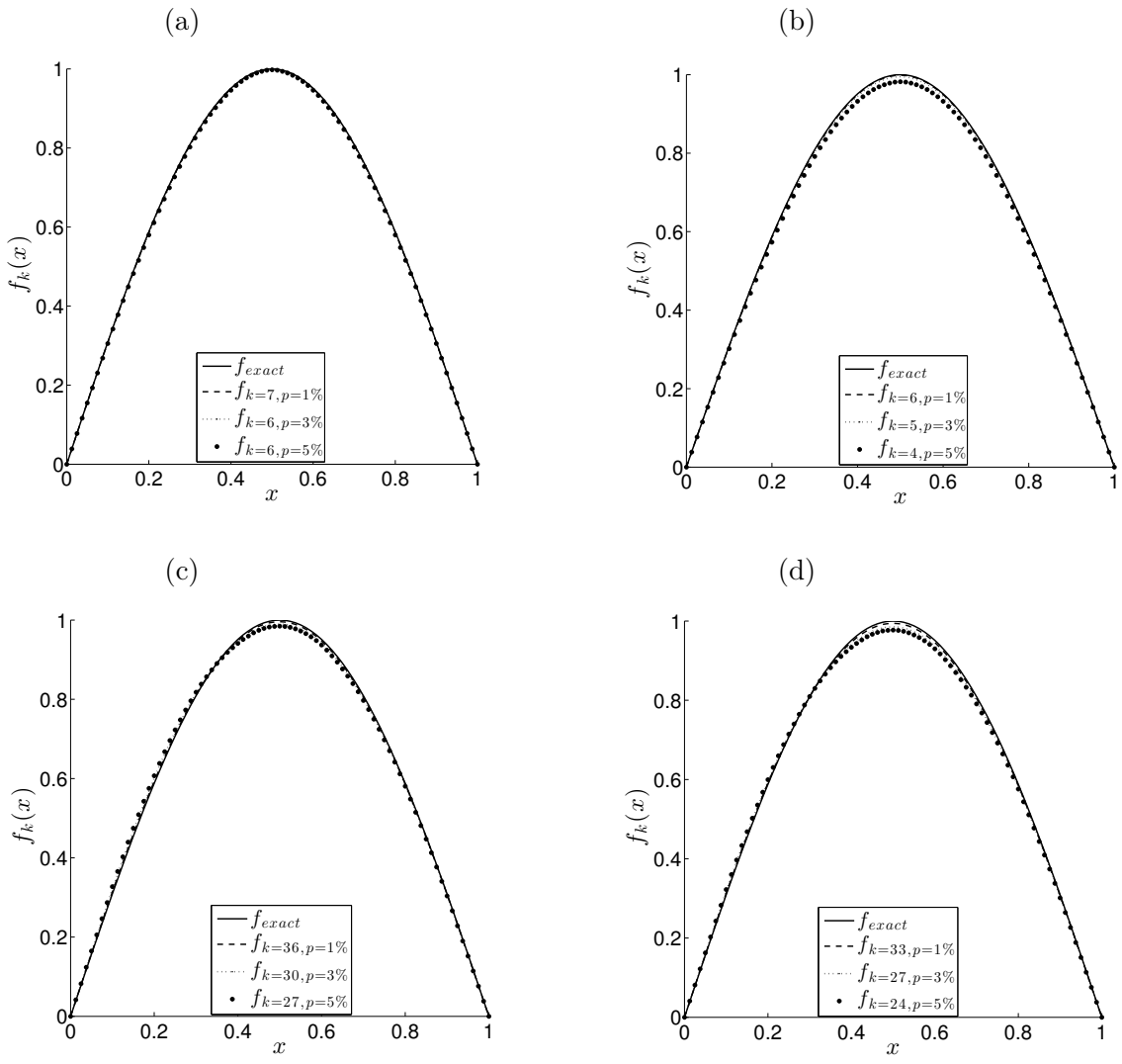

Figure 9: The numerical solution f_k at various iteration numbers k, in comparison with the exact solution (101), for $p \in \{1, 3, 5\}\%$ noise for the inverse problem of Example 2 with the displacement measurement (98) for (a) $k_{opt} \in \{7, 6, 6\}$, (b) $k_{discr} \in \{6, 5, 4\}$, and with the time-average displacement measurement (99) for (c) $k_{opt} \in \{36, 30, 27\}$, (d) $k_{discr} \in \{33, 27, 24\}$.

7.3 Example 3

Consider first the direct problem given by the wave equation (79) with the input data (81),

$$u(x,0) = \varphi(x) = \sin(\pi x), \quad u_t(x,0) = \psi(x) = 0, \quad x \in [0,1], \tag{102}$$

$$g(x,t) = 1 + t, \quad t \in [0,1], \tag{103}$$

$$f(x) = \frac{1}{\tilde{\sigma}\sqrt{2\pi}} \exp\left(-\frac{(x-\mu)^2}{2\tilde{\sigma}^2}\right), \tag{104}$$

where $\tilde{\sigma} = 0.1$ and $\mu = 0.5$. Remark that for this example, the force (104) is a Gaussian normal function with mean μ and standard deviation $\tilde{\sigma}$. As $\tilde{\sigma} \to 0$, expression (104) mimics the Dirac delta distribution $\delta(x - \mu)$.

Unlike in the previous two examples, for the above direct problem an explicit analytical solution for the displacement $u(x,t)$ is not readily available and therefore, the values (5) and (6) of $u(x,1)$ and $\int_0^1 u(x,t)dt$, illustrated in Figures 10(a) and 10(b), respectively, have been obtained numerically using the FDM, at described in subsection 7.1. From these figures, a rapid convergence of the numerical results can be observed.

We next solve the inverse problems using the numerically simulated data with $N = M = 80$ from Figure 10. In the numerical solutions of the direct and adjoint problems of the iterative procedure described in Section 6 we also take $N = M = 80$ and $\gamma = 1$. We deliberately use the same mesh discretisation $N = M = 80$ in order to check for exact data the numerical convergence of the Landweber method proposed in the absence of any numerical discretisation error, the only noise present being the $O(10^{-16})$ double precision computer round-off errors. Note that we do not commit an inverse crime since the initial guess is arbitrary, we also add random noise to the input data and the inverse iterative procedure is totally different than the direct problem solver.

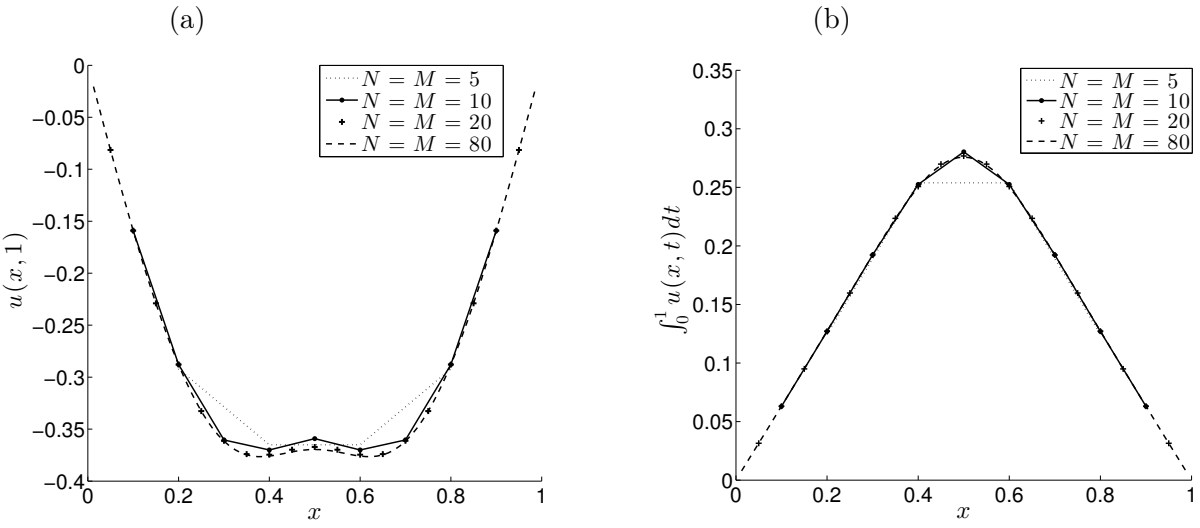

Figure 10: Numerical solution for (a) $u(x,1)$ and (b) $\int_0^1 u(x,t)dt$, for various $N = M \in \{5, 10, 20, 80\}$, for the direct problem of Example 3.

7.3.1 Inverse problems

As in Example 2, the function (103) satisfies $g(x,t) \geq 0, g_t(x,t) > 0, \forall (x,t) \in \overline{Q}_T$ and hence, according to Theorems 1 and 2, both the inverse problems (79), (81), (102) with the input (5) or (6) represented in Figure 10(a) or 10(b), respectively, have unique solutions. First consider the case without noise, i.e. $p = 0$. Figure 11 shows the objective functions (47) and (60), and the corresponding accuracy error (93), versus the number of iterations. Also, Figure 12 shows the convergence of the corresponding numerical solutions, as the number of iterations increases. From both figures it can be seen that the number of iterations necessary to achieve a high level of accuracy is large of $O(10^5)$. It is much larger than in the previous Examples 1 and 2 because the force function (104) to be retrieved has a small standard deviation $\tilde{\sigma}$ and

therefore a sharper peak centred at the mean value $\mu = 0.5$ than the trigonometric functions (83) and (101). By comparing the results in Figures 11 and 12 one can also observe that the convergence for the inverse problem with the displacement measurement (5) is much faster (and for some number of iteration more accurate) than that with time-average displacement measurement (29).

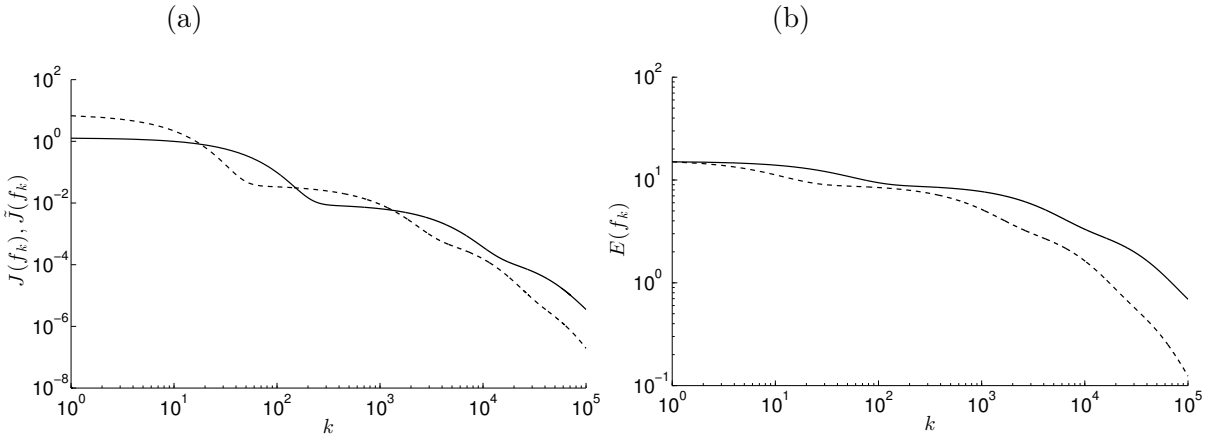

Figure 11: (a) The objective functions $J(f_k)$, $\tilde{J}(f_k)$ and (b) the accuracy error $E(f_k)$, versus the number of iterations $k = \overline{1, 10^5}$, no noise for the inverse problem of Example 3 with the displacement measurement (5) (- - -) and with the time-average displacement measurement (29) (—).

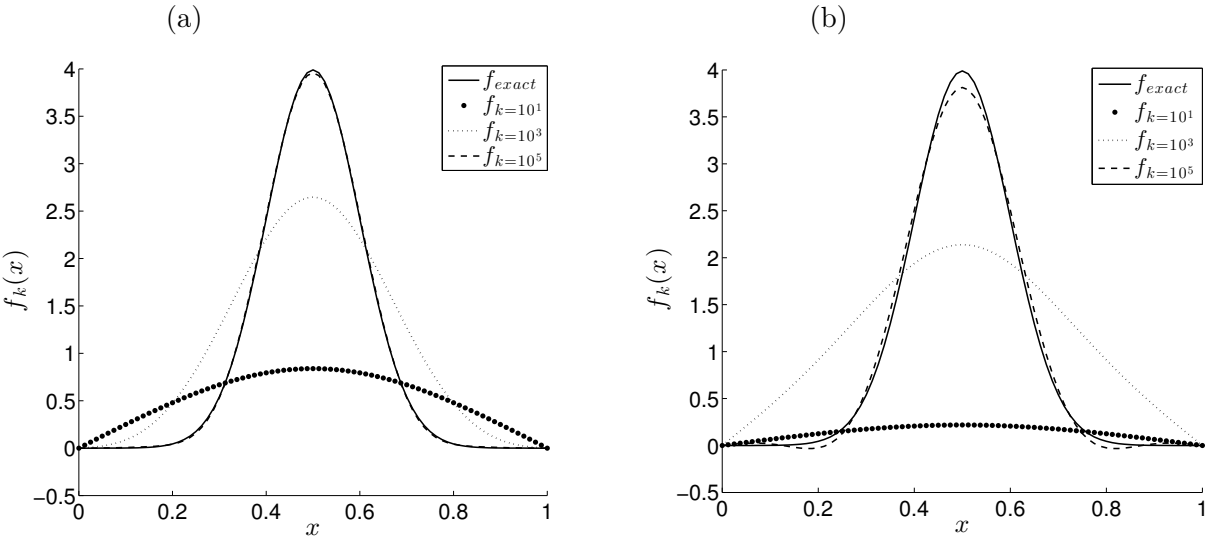

Figure 12: The numerical solution f_k at various iteration numbers k, in comparison with the exact solution (104), no noise for the inverse problem of Example 3 with (a) the displacement measurement (5), and (b) the time-average displacement measurement (29).

Next we add some $p \in \{1, 3, 5\}\%$ noise in the input data with $N = M = 80$ of Figure 10. Figures 13, 14 and Table 3 are analogous to Figures 8, 9 and Table 2 of Example 2 and

similar quantitative conclusions can be drawn in terms of comparing the inverse problems with either the displacement measurement (5) numerically simulated in Figure 10(a) or with the time-average measurement (29) numerically simulated in Figure 10(b). Of course, since more iterations are required for Example 3 than for Example 2, the thresholds k_{discr} and k_{opt} are much higher (and also more different between themselves) in Table 3 than in Table 2. Furthermore, the accuracy of the numerical results in Figure 9 for Example 2 is much higher than that in Figure 14 for Example 3, as expected since the trigonometric source (101) is less complicated than the Gaussian normal bell-shaped function (104).

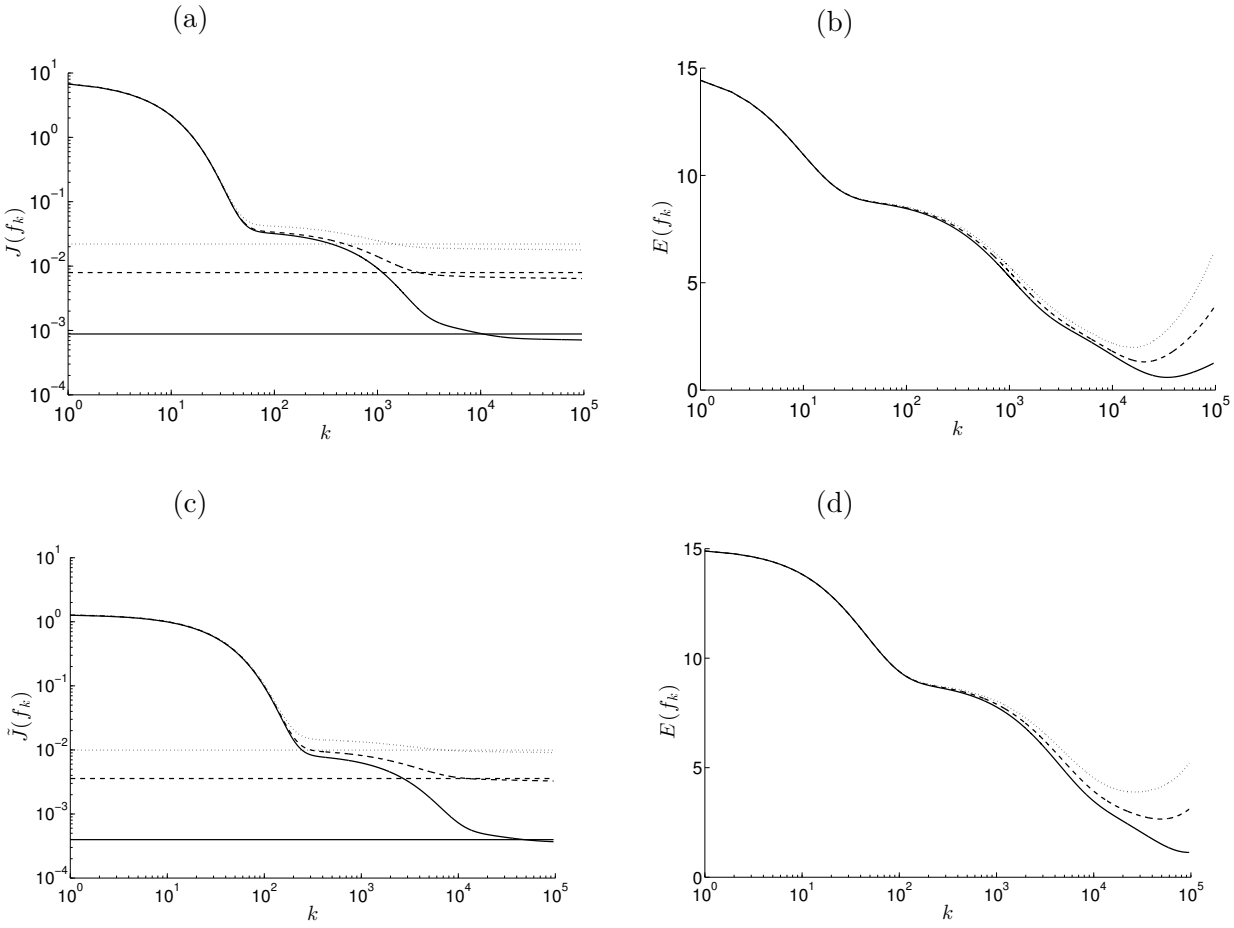

Figure 13: (a) The objective function $J(f_k)$ and (b) the corresponding accuracy error $E(f_k)$ for the inverse problem of Example 3 with the displacement measurement from Figure 10(a) with $N = M = 80$, and (c) the objective function $\tilde{J}(f_k)$ and (d) the corresponding accuracy error $E(f_k)$ for the inverse problem of Example 3 with the time-average displace measurement of Figure 10(b) with $N = M = 80$. All curves are functions of the number of iterations $k = \overline{1, 10^5}$, for $p = 1\%$ (—), $p = 3\%$ (- - -) and $p = 5\%$ ($\cdots$) noise. The horizontal lines in (a) and (c) represent the threshold $\tau^2\epsilon^2/2$ with $\tau = 1.2$ and $\tau = 1.1$, respectively.

Table 3: The stopping iteration number k_{discr} chosen according to the discrepancy principle criterion (78), as illustrated in Figures 13(a), 13(c), and the optimal iteration number k_{opt} chosen according to the minimum of the accuracy error function (93) in Figures 13(b), 13(d), for various percentages of noise $p \in \{1, 3, 5\}\%$ for Example 3 with the displacement measurement from Figure 10(a) with $N = M = 80$ and $\tau = 1.2$ (upper part of the table) and with the time-average displacement measurement from Figure 10(b) with $N = M = 80$ and $\tau = 1.1$ (lower part of the table). The corresponding accuracy errors $E(f_{k_{discr}})$ and $E(f_{k_{opt}})$ are also included.

p	1%	3%	5%
k_{opt}	34080	20363	15577
$E(f_{k_{opt}})$	0.5899	1.3122	1.9840
k_{discr}	17712	7949	7012
$E(f_{k_{discr}})$	0.9448	2.0762	2.5206
k_{opt}	95908	49208	26760
$E(f_{kopt})$	1.1314	2.6532	3.8913
k_{discr}	64996	35905	14998
$E(f_{kdiscr})$	1.2761	2.7219	4.1004

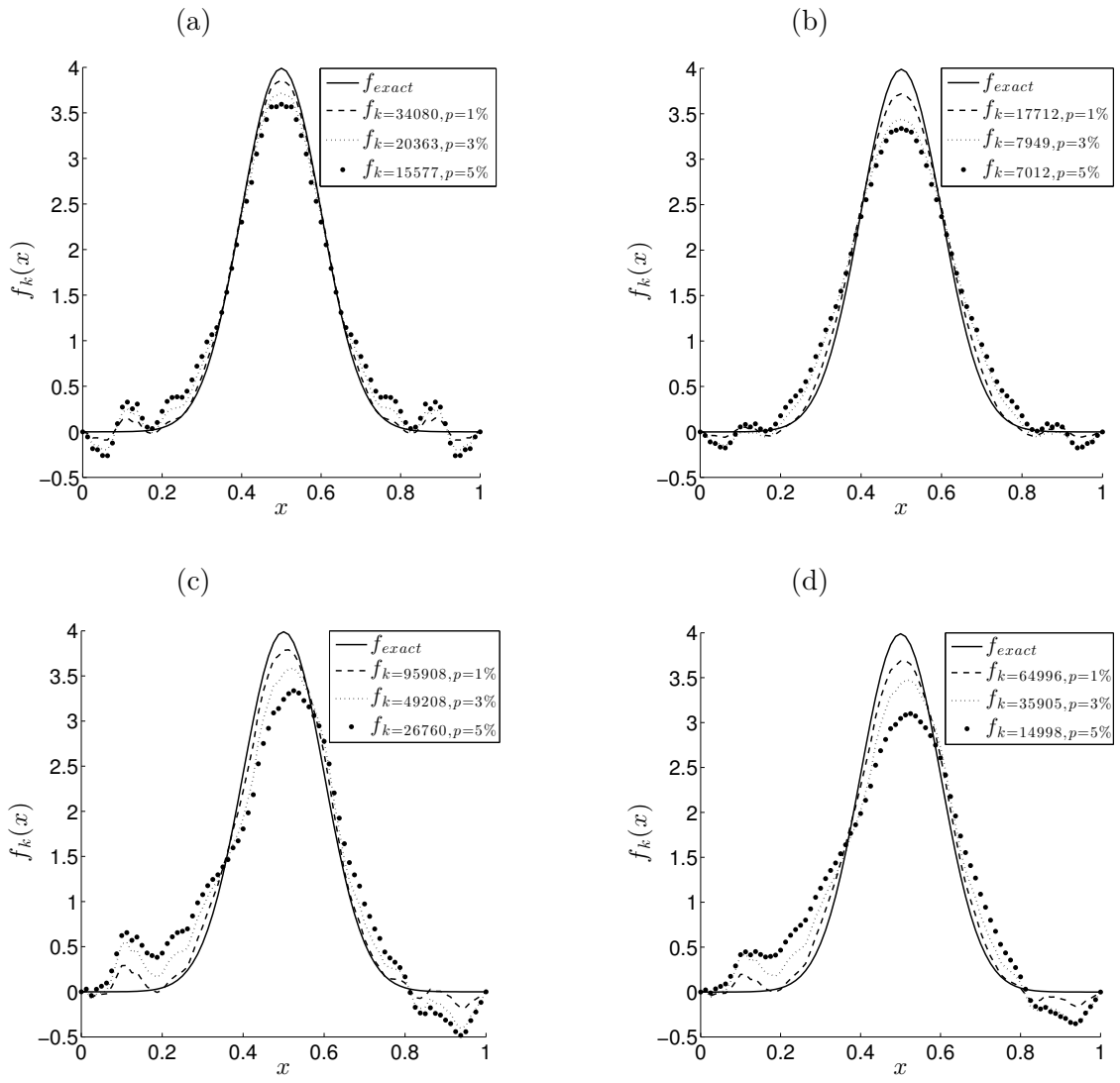

Figure 14: The numerical solution f_k at various iteration numbers k, in comparison with the exact solution (104), for $p \in \{1, 3, 5\}\%$ noise for the inverse problem of Example 3 with the displacement measurement from Figure 10(a) with $N = M = 80$ for (a) $k_{opt} \in \{34080, 20363, 15577\}$, (b) $k_{discr} \in \{17712, 7949, 7012\}$, and with the time-average displacement measurement from Figure 10(b) with $N = M = 80$ for (c) $k_{opt} \in \{95908, 49208, 26760\}$, (d) $k_{discr} \in \{64996, 35905, 14998\}$.

7.4 Example 4

Consider first the direct problem given by the wave equation (79) with the input data (81),

$$u(x, 0) = \varphi(x) = 0, \quad u_t(x, 0) = \psi(x) = 0, \quad x \in [0, 1], \tag{105}$$

$$g(x, t) = 1 + t, \quad t \in [0, 1], \tag{106}$$

$$f(x) = \begin{cases} x & \text{if} \quad 0 \le x \le \frac{1}{2}, \\ 1 - x & \text{if} \quad \frac{1}{2} < x \le 1. \end{cases} \tag{107}$$

Remark that for this example, the force (107) has a triangular shape, being continuous but non-differentiable at the peak $x = 1/2$. This example also does not possess an explicit analytical solution for the displacement $u(x,t)$ being readily available.

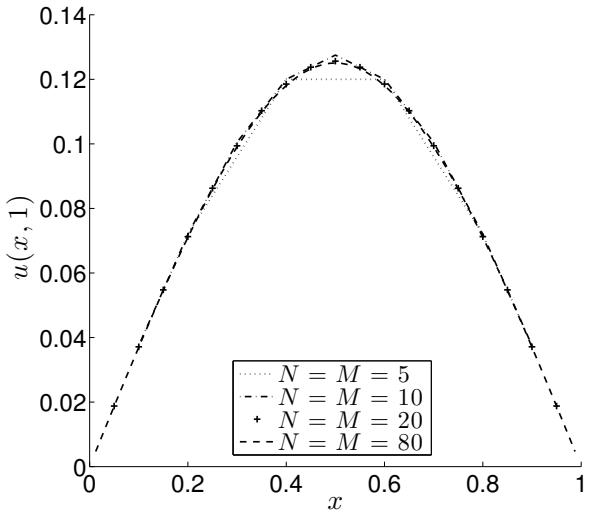

Figure 15: Numerical solution for $u(x,1)$, for various $N = M \in \{5, 10, 20, 80\}$, for the direct problem of Example 4.

Figure 15 shows the rapid convergence of the FDM numerical solution $u(x,1)$ of the direct problem (79), (81) and (105), as $N = M$ increases. The numerically simulated $u(x,1)$ with $N = M = 80$ is used as input data (5) in the inverse problem (79), (81), (105) whose existence and uniqueness of solution is guaranteed from Theorem 1 since $g(x,t)$ given by (106) satisfies $g(x,t) \geq 0, g_t(x,t) > 0, \forall (x,t) \in \overline{Q}_T$. We fix $N = M = 80$ and $\gamma = 1$.

It was observed in Example 3 and else where that the convergence of the Landweber iterative method described in Section 6 can become prohibitely show. One way to increase the rate of convergence is to increase the value of the relaxation parameter γ in (74) and we shall investigate this effect for the next Example 5. Alternatively, one can speed up the convergence of the minimization of the least-squares functional (47) or (60) by employing the convergent and regularizing conjugate gradient method (CGM) for the stable reconstruction of the displacement u and force f. In addition, the CGM does not require any choice of a relaxation parameter γ, as the Landweber method does in order to iterate in formula (74). Similarly, as described in [8, 12] for the heat equation, this algorithm runs as follows:

Let steps (i) and (ii) be the same as in the algorithm of Section 6. The next steps are as follows:

(iii) Calculate

$$d_k(x) = -z_k(x) + \beta_{k-1} d_{k-1}(x), \tag{108}$$

with the convention that $\beta_{-1} = 0$ and

$$\beta_{k-1} = \frac{||z_k||^2_{L^2(\Omega)}}{||z_{k-1}||^2_{L^2(\Omega)}}, \quad k \geq 1 \tag{109}$$

(iv) Solve the direct problem (1)-(4) with $\varphi = \psi = 0$ and $f = d_k$ to determine $A_0 d_k$ or $\tilde{A}_0 d_k$, where the operators A_0 and $\tilde{A}_0$ have been defined in Section 3. Set the direction search

$$\alpha_k = \frac{||z_k||^2_{L^2(\Omega)}}{||A_0 d_k||^2_{L^2(\Omega)}}, \quad \text{or} \quad \alpha_k = \frac{||z_k||^2_{L^2(\Omega)}}{||\tilde{A}_0 d_k||^2_{L^2(\Omega)}}, \quad k \geq 0, \tag{110}$$

and pass to the new iteration by letting

$$f_{k+1}(x) = f_k(x) + \alpha_k d_k(x). \tag{111}$$

(v) Let u_{k+1} solve the direct problem (1)-(4) with $f = f_{k+1}$ and go back (repeat) steps (ii)-(iv) until the discrepancy principle stopping criterion (78) is satisfied.

Note that for $\Omega = (0, L)$ the $L^2(0, L)$ integrals in (109) and (110) are calculated using the trapezoidal rule which, for the homogeneous Dirichlet boundary data (81), is given by

$$||z_k||^2_{L^2(0,L)} = (\Delta x) \sum_{i=1}^{M-1} z_k^2(x_i), \tag{112}$$

and a similar expression exists for $||A_0 d_k||^2_{L^2(0,L)}$.

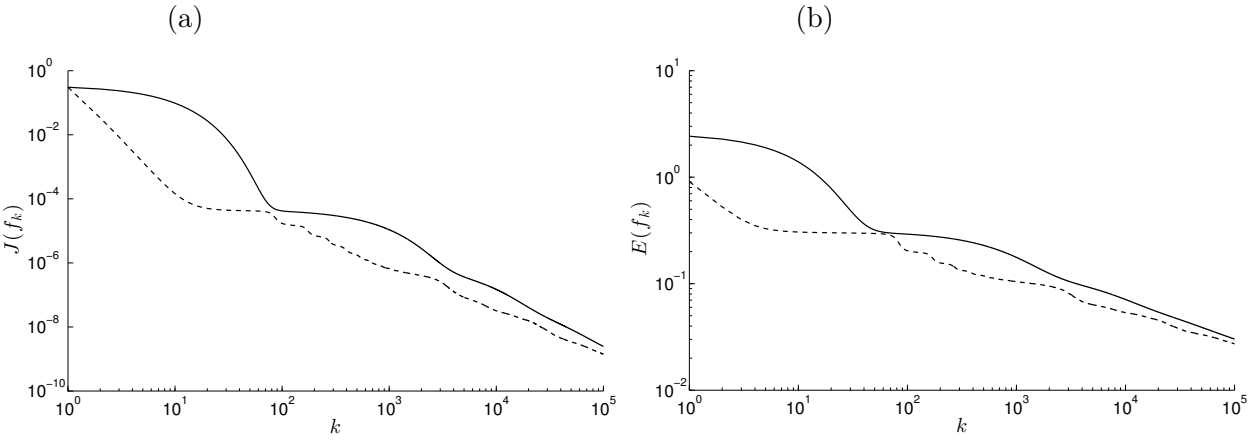

Figure 16: (a) The objective function $J(f_k)$ and (b) the accuracy error $E(f_k)$, versus the number of iterations $k = \overline{1, 10^5}$, obtained using the Landweber method (—) and the CGM (- - -), no noise for the inverse problem of Example 4.

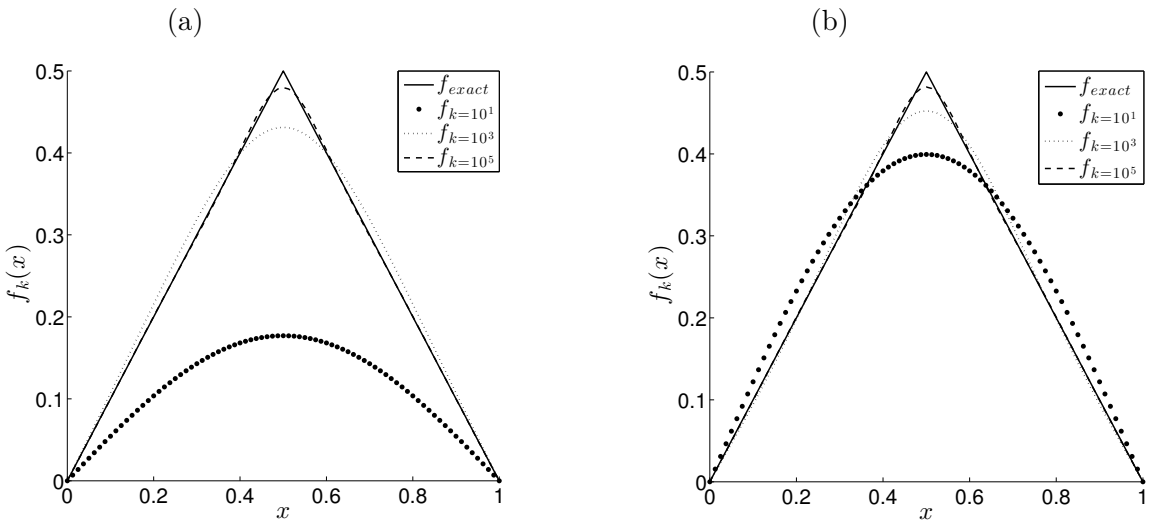

Figure 17: Numerical solution f_k for various iteration numbers $k \in \{10^1, 10^3, 10^5\}$, in comparison with the exact solution (107), obtained using (a) the Landweber method and (b) the CGM, no noise for the inverse problem of Example 4.

The objective function (47), the accuracy error (93) and the numerical solution for the force at various iteration numbers obtained using the Landweber method and the CGM are plotted in Figures 16(a), 16(b) and 17, respectively. From these figures it can be seen that it takes a large number of iterations of $O(10^5)$ to converge with a good accuracy to the exact solution (107), similarly to what happened for Example 3, when the Lanweber method is employed. In comparison to the previous Examples 1 and 2 this is to be expected because the force function (107) to be retrieved is non-smooth possessing a sharp corner at the peak $x = 1/2$. Moreover, the behaviour of the convergence is similar to that of Example 3 for which the Gaussian normal force function (104) to be retrieved, although smooth, it possesses also a sharp peak at $x = 1/2$.

On the other hand, the convergence is much faster when the CGM is employed. When we add some $p \in \{1, 3, 5\}\%$ noise in the input data (5), the conclusions are similar to those drawn from Example 3 if one compares Figures 18, 19 and Table 4 with Figures 13, 14 and the upper part of Table 3. Furthermore, the numerical details included in Table 4 show that the CGM is about 10 times faster than the Landweber method.

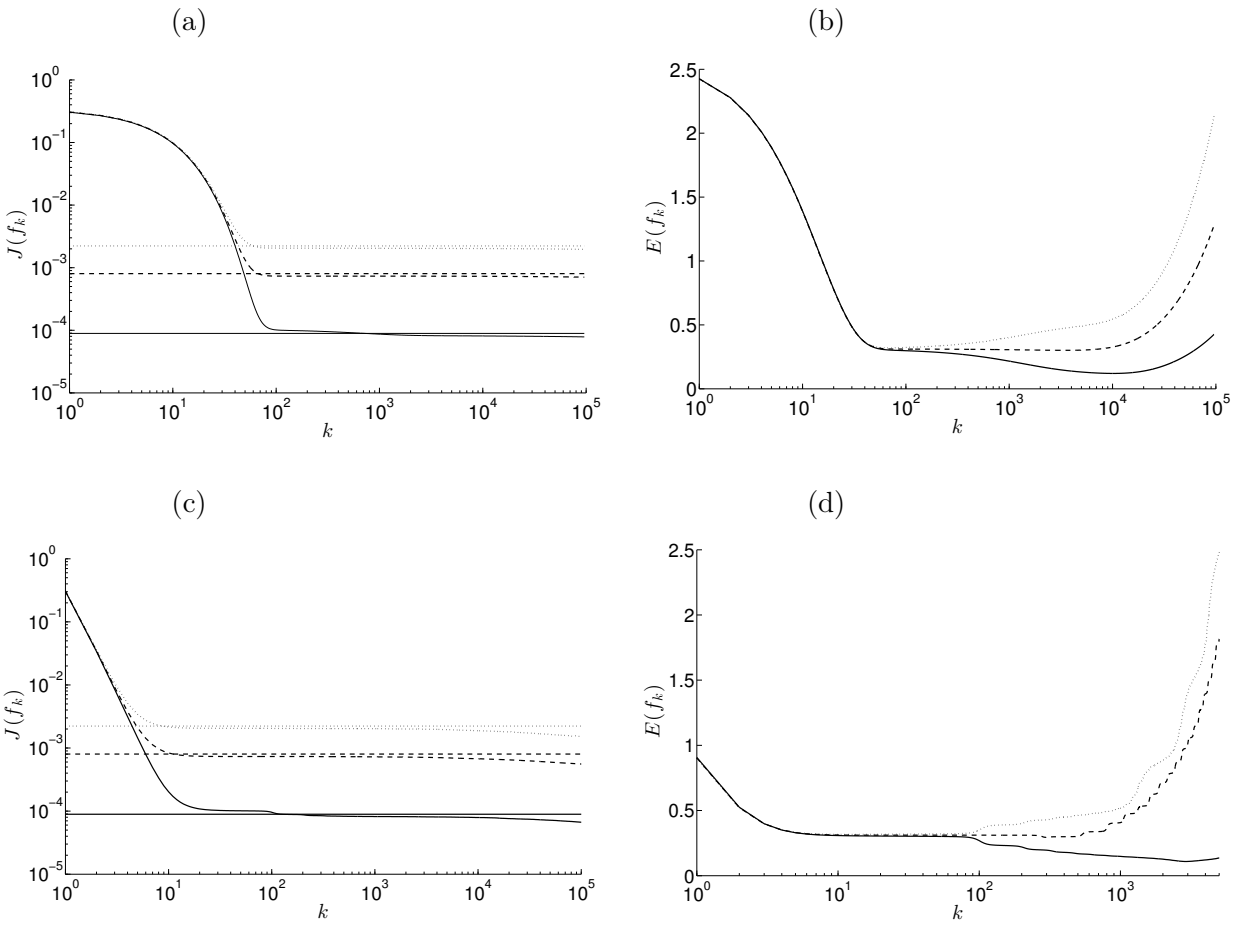

Figure 18: (a) and (c) The objective function $J(f_k)$, and (b) and (d) the accuracy error $E(f_k)$, versus the number of iterations $k = \overline{1, 10^5}$, obtained using the Landweber and CGM methods, respectively, for $p = 1\%$ (—), $p = 3\%$ (- - -) and $p = 5\%$ ($\cdots$) noise for the inverse problem of Example 4. The horizontal lines represents the threshold $\tau^2 \frac{\epsilon^2}{2}$ with $\tau = 1.15$.

Table 4: The stopping iteration numbers k_{discr} chosen according to the discrepancy principle criterion (78) (with $\tau = 1.15$), as illustrated in Figures 18(a) and 18(c), and the optimal iteration numbers k_{opt} chosen according to the minimum of the accuracy error function (93) in Figures 18(b) and 18(d), for various percentages of noise $p \in \{1, 3, 5\}\%$ for Example 4. The corresponding accuracy errors $E(f_{k_{discr}})$ and $E(f_{k_{opt}})$ are also included. The CGM results are included in brackets

p	1%	3%	5%
k_{opt}	10171 (2908)	3429 (295)	68 (12)
$E(f_{k_{opt}})$	0.1202 (0.1090)	0.3009 (0.2943)	0.3198 (0.3167)
k_{discr}	2995 (130)	95 (21)	70 (11)
$E(f_{k_{discr}})$	0.1507 (0.2341)	0.3105 (0.3108)	0.3199 (0.3168)

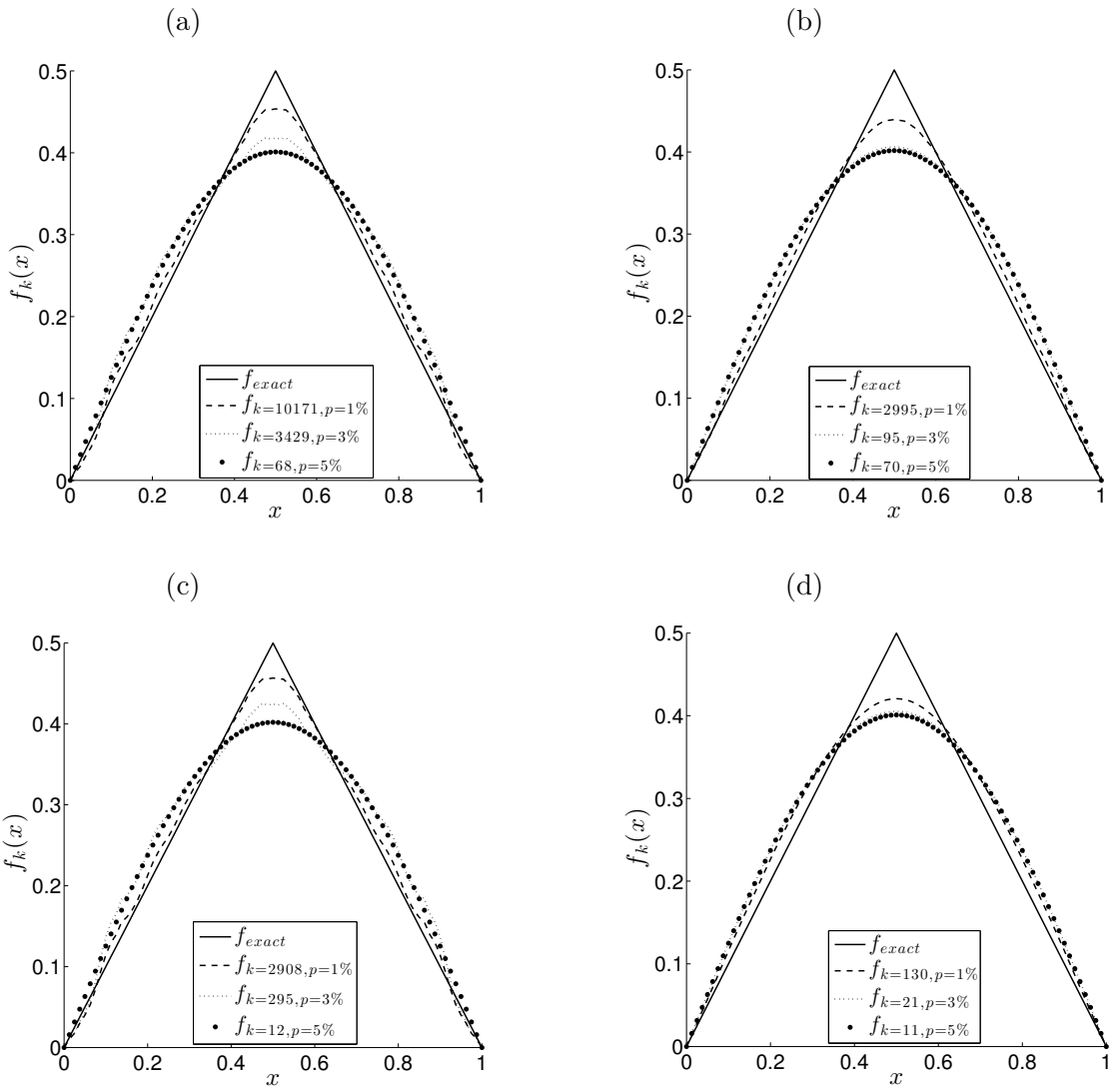

Figure 19: The exact solution f in comparison with numerical solution f_k for (a) and (c) $k_{opt} \in \{10171, 3429, 68\}$ and $k_{opt} \in \{2908, 295, 12\}$, and (b) and (d) $k_{discr} \in \{2995, 95, 70\}$ and $k_{discr} \in \{130, 21, 11\}$, obtained using the Landweber and CGM methods, respectively, for $p \in \{1, 3, 5\}\%$ noise for the inverse problem of Example 4.

We finally note that similar results have been obtained for the inverse problem given by equations (79), (81), (105) with the integral measurement (29) and therefore, they are not presented.

7.5 Example 5

The previous example investigated a severe test given by the non-smooth triangular shape force function (107). In this subsection, we consider an even more severe test example given by the discontinuous force

$$f(x) = \begin{cases} 0 & \text{if} \quad 0 \le x < \frac{1}{3}, \\ 1 & \text{if} \quad \frac{1}{3} \le x \le \frac{2}{3}, \\ 0 & \text{if} \quad \frac{2}{3} < x \le 1. \end{cases} \tag{113}$$

We take the same input data (105) and (106), as in Example 4. Then, on solving the direct problem given by equations (79), (81), (105) with the forcing term given by the product of the functions in (106) and (113), we obtain the numerical results for the time-average displacement $\int_0^1 u(x,t)dt$ illustrated in Figure 20. From this figure it can be seen that a convergent FDM numerical solution is achieved.

For brevity, in what follows we only illustrate the numerical results obtained for the inverse problem (1)-(4), (29), noting that similar results have been obtained for the inverse problem (1)-(5).

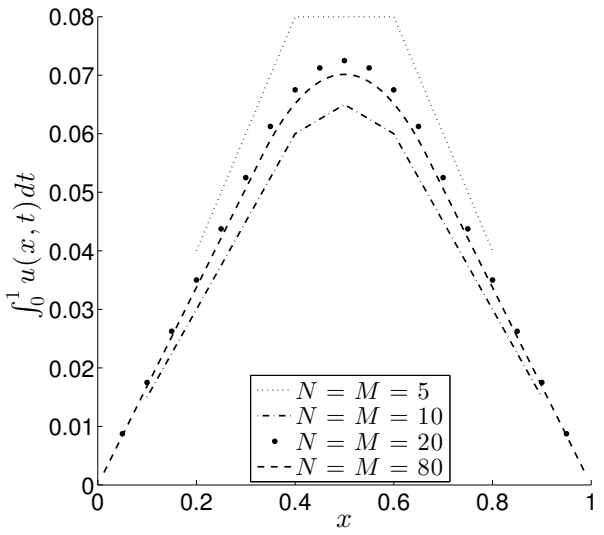

Figure 20: Numerical solution for $\int_0^1 u(x,t)dt$, for various $N = M \in \{5, 10, 20, 80\}$, for the direct problem of Example 5.

The numerically simulated data for $\int_0^1 u(x,t)dt$ obtained with $N = M = 80$ is used as input (6) in the inverse problem given by equations (79), (81) and (105). Again, as in Examples 2 and 3 the function g given by equation (103) (or (106)) satisfies $0 \not\equiv g(x,t) \geq 0, \forall (x,t) \in \overline{Q}_T$ and hence, according to Theorem 2, the inverse problem has a unique solution. As expected, for exact data a very slow convergence of the objective function (60) is encountered by the Landweber iteration method because the force function (113) to be retrieved is discontinuous at the points $x \in \{1/3, 2/3\}$. In fact, we had to increase the value of the relaxation factor γ in order to achieve convergence in a reasonable number of iterations.

Figure 21 shows the objective function (60) and the accuracy error (93), versus the number of iterations $k = \overline{1, 10^5}$, for various values of the relaxation parameter $\gamma \in \{1, 5, 15\}$. From this figure it can be seen that the rate of convergence increases as we increase γ from 1 to 5 and then to 15. The corresponding numerical solutions for the force $f_k(x)$ are shown in Figure 22 for various numbers of iterations $k \in \{10^1, 10^3, 10^5\}$, and again more accurate results are obtained as we increase k and/or γ.

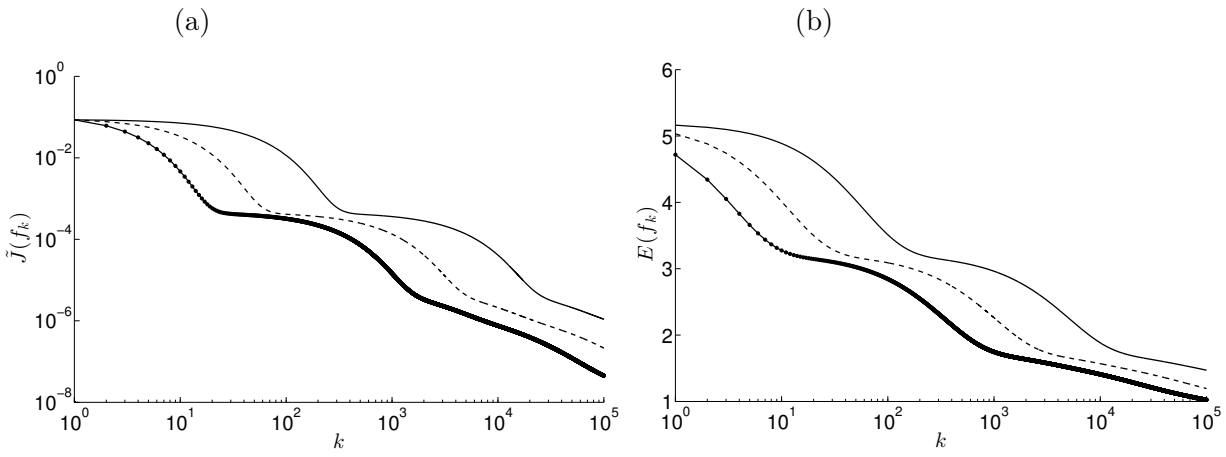

Figure 21: (a) The objective function $\tilde{J}(f_k)$ and (b) the accuracy error $E(f_k)$, versus the number of iterations $k = \overline{1, 10^5}$, for various $\gamma = 1$ (—), $\gamma = 5$ (- - -) and $\gamma = 15$ ($-\bullet-$), no noise for the inverse problem of Example 5.

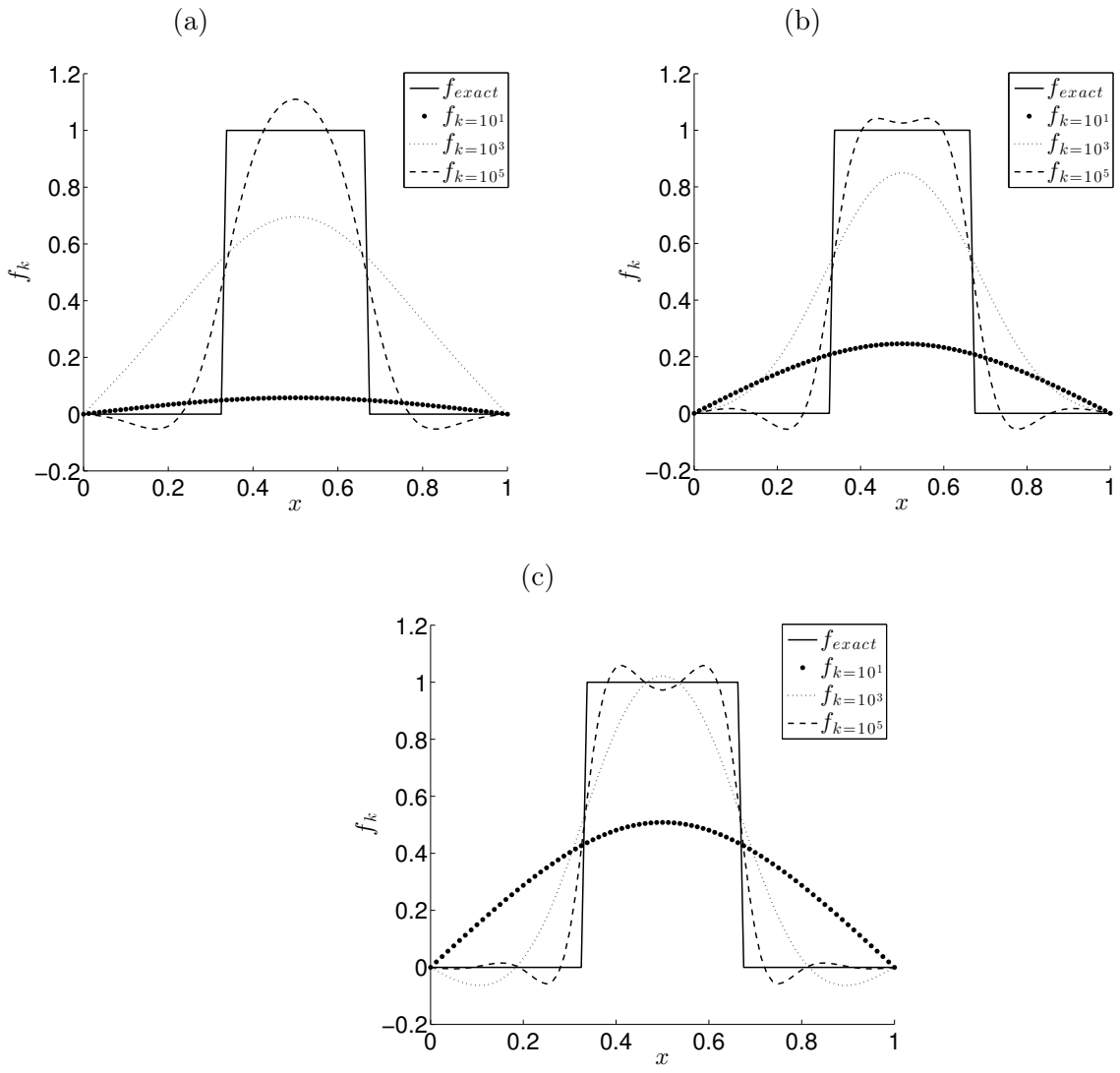

Figure 22: Numerical solution f_k for various iteration numbers $k \in \{10^1, 10^3, 10^5\}$, in comparison with the exact solution (113), for (a) $\gamma = 1$, (b) $\gamma = 5$ and (c) $\gamma = 15$, no noise for the inverse problem of Example 5.

In order to investigate the stability of the numerical solution we include some $p \in \{1, 3, 5\}\%$ noise into the input data, as given by equation (94), and the numerical results obtained with $\gamma = 15$ are presented in Figures 23, 24 and Table 5. As in the previous examples, Figure 23 and Table 5 justify the choice of the stopping iteration number k_{discr} and furthermore, the numerical solutions illustrated in Figure 24 show that stable and reasonably accurate results are obtained for recovering the severely discontinuous force function (113).

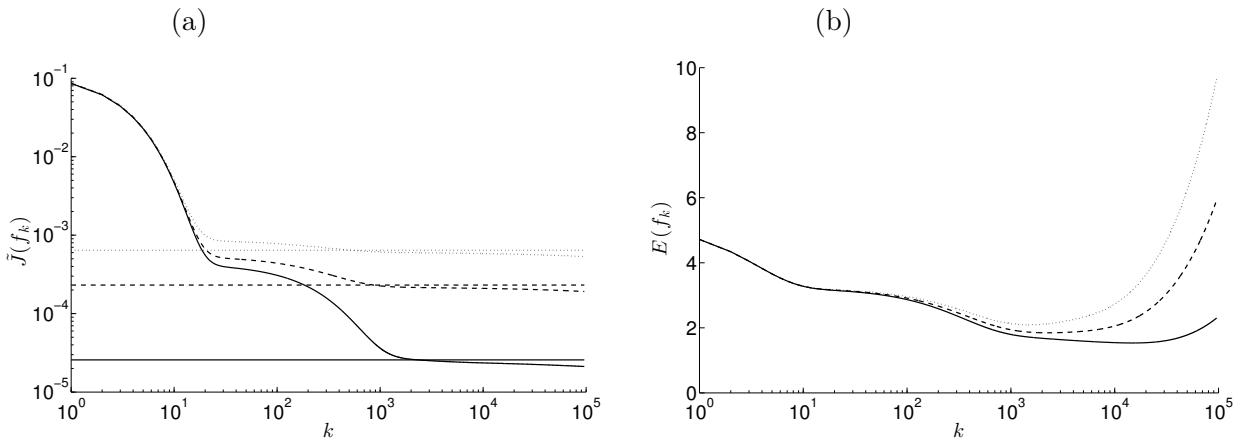

Figure 23: (a) The objective function $\tilde{J}(f_k)$ and (b) the accuracy error $E(f_k)$, versus the number of iterations $k = \overline{1, 10^5}$, for $p = 1\%$ (—), $p = 3\%$ (- - -) and $p = 5\%$ ($\cdots$) noise for the inverse problem of Example 5 obtained with $\gamma = 15$. The horizontal lines represents the threshold $\tau^2 \frac{\epsilon^2}{2}$ with $\tau = 1.1$.

Table 5: The stopping iteration number k_{discr} chosen according to the discrepancy principle criterion (78) (with $\tau = 1.1$), as illustrated in Figure 23(a), and the optimal iteration number k_{opt} chosen according to the minimum of the accuracy error function (93) in Figure 23(b), for various percentages of noise $p \in \{1, 3, 5\}\%$ for Example 5 obtained with $\gamma = 15$. The corresponding accuracy errors $E(f_{k_{discr}})$ and $E(f_{k_{opt}})$ are also included.

p	1%	3%	5%
k_{opt}	14823	2275	1523
$E(f_{k_{opt}})$	1.5342	1.8471	2.0906
k_{discr}	9599	2000	1000
$E(f_{k_{discr}})$	1.5466	1.8488	2.1319

In the next section we present a numerical extension to two-dimensions.

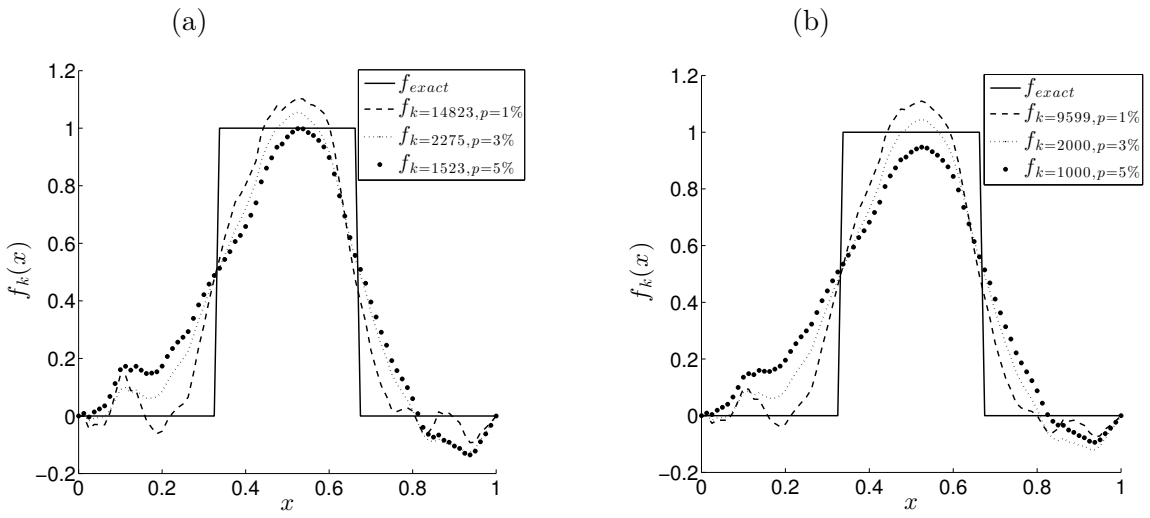

Figure 24: The exact solution (113) for f in comparison with the numerical solution f_k for (a) $k_{opt} \in \{14823, 2275, 1523\}$ and (b) $k_{discr} \in \{9599, 2000, 1000\}$, for $p \in \{1, 3, 5\}\%$ noise for the inverse problem of Example 5 obtained with $\gamma = 15$.

8 Two-dimensions

In this section, we consider the initial boundary value problem (1)-(4) in two-dimensions, i.e. $n = 2$ and $\Omega = (0, L) \times (0, L)$ with $L > 0$, given by

$$u_{tt}(x, y, t) = u_{xx}(x, y, t) + u_{yy}(x, y, t) + f(x, y)g(x, y, t), \quad (x, y, t) \in (0, L) \times (0, L) \times (0, T], \tag{114}$$

$$u(x, y, 0) = \varphi(x, y), \quad u_t(x, y, 0) = \psi(x, y), \quad (x, y) \in (0, L) \times (0, L), \tag{115}$$

$$u(x, y, t) = 0, \quad (x, y) \in \partial\Omega \times (0, T). \tag{116}$$

The discrete form of this direct problem is as follows. We divide the solution domain $(0, L) \times (0, L) \times (0, T)$ into M, N and K subintervals of equal space lengths Δx, Δy and time step Δt, where $\Delta x = L/M$, $\Delta y = L/N$ and $\Delta t = T/K$. We denote $u_{i,j,k} = u(x_i, y_j, t_k)$, where $x_i = i\Delta x$, $y_j = j\Delta y$, $t_k = k\Delta t$, and $f_{i,j} = f(x_i, y_j)$, $g_{i,j,k} = g(x_i, y_j, t_k)$ for $i = \overline{0, M}$, $j = \overline{0, N}$, $k = \overline{0, K}$. Then, a central-difference approximation to equations (114)-(116) at the mesh points $(x_i, y_j, t_k) = (i\Delta x, j\Delta y, k\Delta t)$ is

$$u_{i,j,k+1} = r_x(u_{i+1,j,k} + u_{i-1,j,k}) + r_y(u_{i,j+1,k} + u_{i,j-1,k}) + 2r_{xy1}u_{i,j,k} - u_{i,j,k-1} + (\Delta t)^2 f_{i,j}g_{i,j,k}, \quad i = \overline{1, (M-1)}, \quad j = \overline{1, (N-1)}, \quad k = \overline{1, (K-1)}, \tag{117}$$

$$u_{i,j,0} = \varphi(x_i, y_j), \quad i = \overline{0, M}, \quad j = \overline{0, N},$$
$$\frac{u_{i,j,1} - u_{i,j,-1}}{2\Delta t} = \psi(x_i, y_j), \quad i = \overline{1, (M-1)}, \quad j = \overline{1, N-1}, \tag{118}$$

$$u_{0,j,k} = u_{M,j,k} = u_{i,0,k} = u_{i,N,k} = 0, \quad i = \overline{1, (M-1)}, \quad j = \overline{1, (N-1)}, \quad k = \overline{1, K}, \tag{119}$$

where $r_x = \frac{(\Delta t)^2}{(\Delta x)^2}$, $r_y = \frac{(\Delta t)^2}{(\Delta y)^2}$, and $r_{xy1} = 1 - r_x - r_y$. This is an explicit formula which is stable if $\frac{4(\Delta t)^2}{(\Delta x)^2+(\Delta y)^2} \leq 1$, giving approximation values for the solution at mesh points along $t = 2\Delta t, 3\Delta t, ...$, as soon as the mesh values along $t = \Delta t$ have been determined. Putting $j = 0$ in equation (117) and using (118), we obtain

$$\begin{aligned} u_{i,j,1} &= \frac{r_x}{2}(\varphi(x_{i+1}, y_j) + \varphi(x_{i-1}, y_j)) + \frac{r_x}{2}(\varphi(x_i, y_{j+1}) + \varphi(x_i, y_{j-1})) + r_{xy1}\varphi(x_i, y_j) \\ &+ (\Delta t)\psi(x_i, y_j) + \frac{1}{2}(\Delta t)^2 f_{i,j} g_{i,j,0}, \quad i = \overline{1, (M-1)}, \quad j = \overline{1, N-1}. \end{aligned} \tag{120}$$

8.1 Example 6

Consider first the direct problem given by the two-dimensional wave equation (114) with $L = T = 1$, the initial conditions (115) given by

$$\begin{aligned} u(x, y, 0) = \varphi(x, y) = 2\sin(\pi x)\sin(\pi y), \quad u_t(x, y, 0) = \psi(x, y) = 0, \\ x \in [0, 1], \ y \in [0, 1], \end{aligned} \tag{121}$$

and the homogenous Dirichlet boundary conditions (116) given by

$$u(0, y, t) = u(1, y, t) = u(x, 0, t) = u(x, 1, t) = 0, \quad x \in (0, 1), \ y \in (0, 1), \ t \in (0, 1), \tag{122}$$

when

$$g(x, y, t) = 2 + \cos(\pi t), \quad (x, y, t) \in (0, 1) \times (0, 1) \times (0, 1), \tag{123}$$

$$f(x, y) = \pi^2 \sin(\pi x)\sin(\pi y), \quad (x, y) \in (0, 1) \times (0, 1). \tag{124}$$

The exact solution is given by

$$u(x, y, t) = \sin(\pi x)\sin(\pi y)\left(1 + \cos(\pi t)\right), \quad (x, y, t) \in [0, 1] \times [0, 1] \times [0, 1]. \tag{125}$$

The time-average displacement (62) is given by

$$U_T(x, y) = \int_0^1 u(x, y, t)dt = \sin(\pi x)\sin(\pi y), \quad (x, y) \in (0, 1) \times (0, 1). \tag{126}$$

This example is similar in behaviour to the one-dimensional Example 1. The absolute errors between (126) and the numerical values obtained using the trapezoidal rule approximation

$$\begin{aligned} \int_0^1 u(x_i, y_j, t)dt = \frac{\Delta t}{2}\left(\varphi(x_i, y_j) + 2\sum_{k=1}^{K-1} u(x_i, y_j, t_k) + u(x_i, y_j, t_K)\right), \\ i = \overline{1, M-1}, j = \overline{1, N-1} \end{aligned} \tag{127}$$

are shown in Figure 25, and one can observe that an excellent agreement and convergence are obtained.

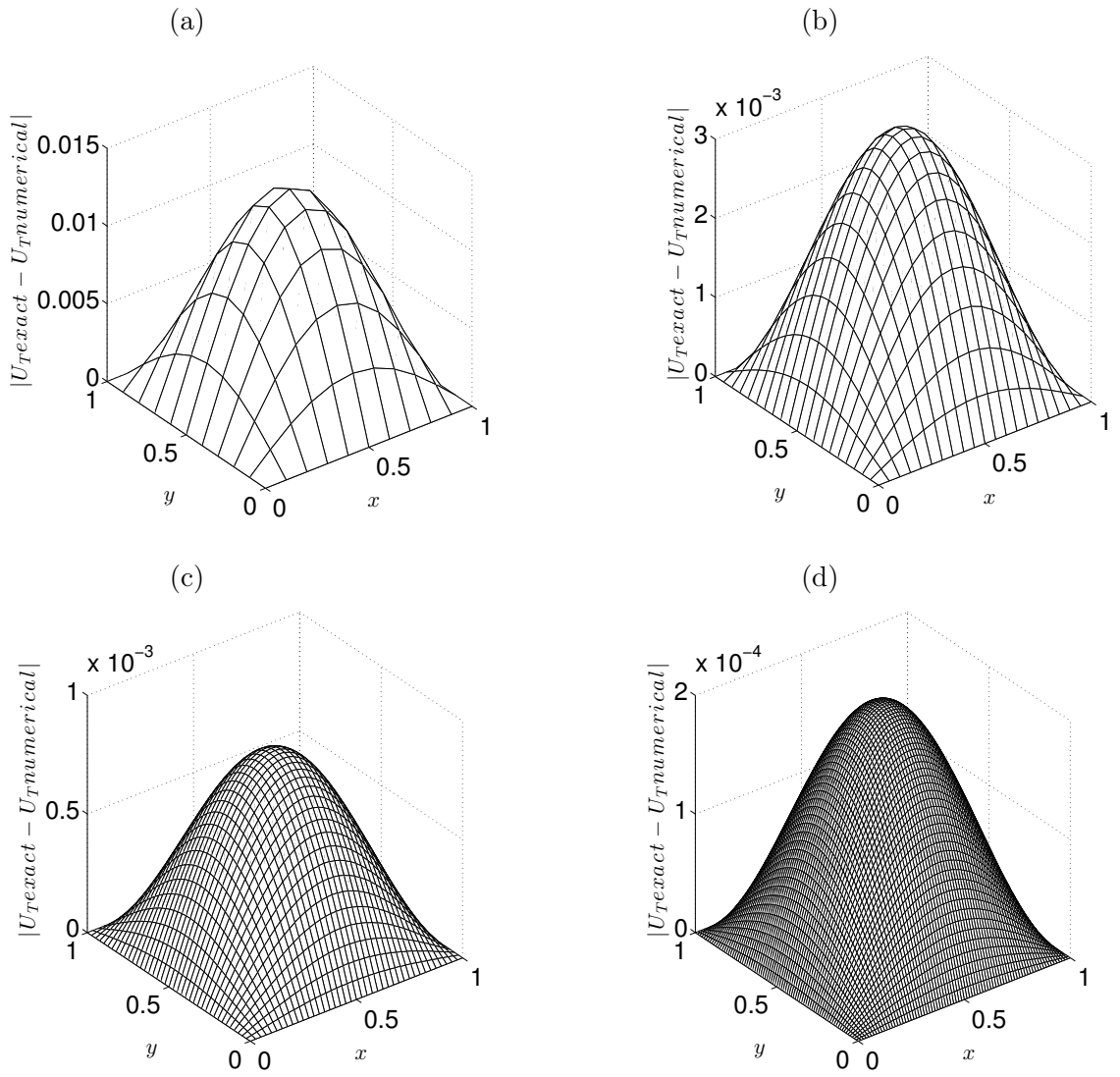

Figure 25: The absolute errors between the exact (126) and numerical solutions (127) for $\int_0^1 u(x, y, t)dt$ for various $N = M \in \{10, 20, 40, 80\}$ and $K = 2N \in \{20, 40, 80, 160\}$ in (a)-(d), respectively, for the direct problem of Example 6.

8.1.1 Inverse problem

In this subsection, we consider solving the inverse problem given by the wave equation (114) with g given by (123), subject to the initial conditions (121), the homogeneous Dirichlet boundary conditions (122) and the additional time-average displacement measurement (126) using the FDM with $N = M = 80$, $K = 160$ and the iterative Landweber method described in Section 6 with the relaxation parameter $\gamma = 1$. The analytical solution of the above inverse problem of Example 6 is given by equations (124) and (125).

The objective function (60) given by

$$\tilde{J}(f_k) = \frac{1}{2}||\xi_k||^2 = \frac{1}{2}\sum_{i=1}^{M-1}\sum_{j=1}^{N-1}\xi_k^2(x_i, y_j), \tag{128}$$

where ξ_k is given by (72), is plotted in Figure 26(a), as a function of the number of iterations

k. Whilst Figure 26(b) shows the accuracy error

$$E(f_k) = ||f_{exact} - f_k|| = \sqrt{\sum_{i=1}^{M-1}\sum_{j=1}^{N-1}(f(x_i, y_j) - f_k(x_i, y_j))^2}. \tag{129}$$

From these figures it can be seen that convergence of both functions (128) and (129) is achieved in about 300 to 500 iterations.

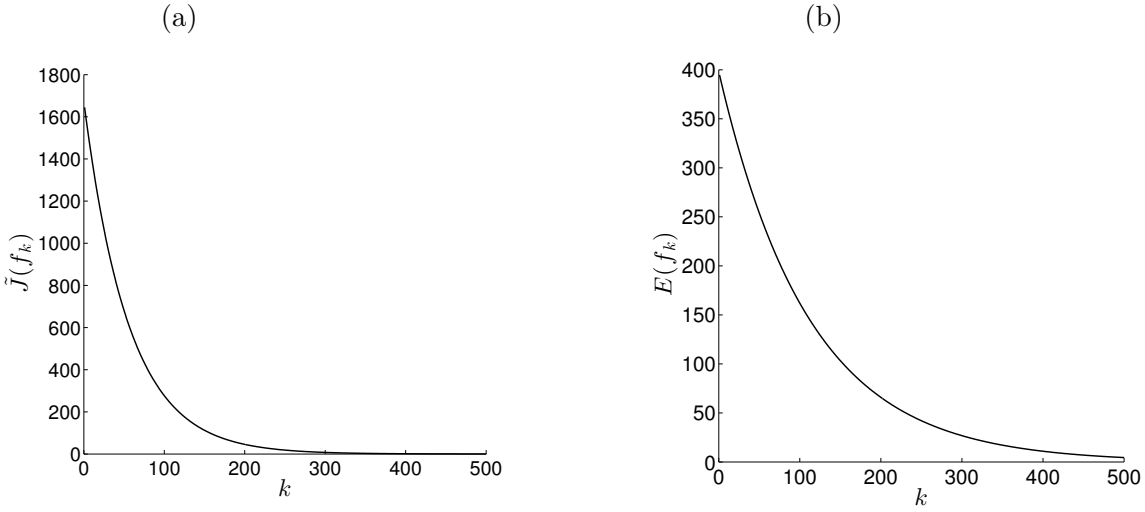

Figure 26: (a) The objective function (128) and (b) the accuracy error (129), versus the number of iterations $k = \overline{1, 500}$, no noise for the inverse problem of Example 6.

Figure 27 shows the numerical force solution f_k at various iteration numbers k and a monotonic increasing convergence to the exact solution (124) can be clearly observed.

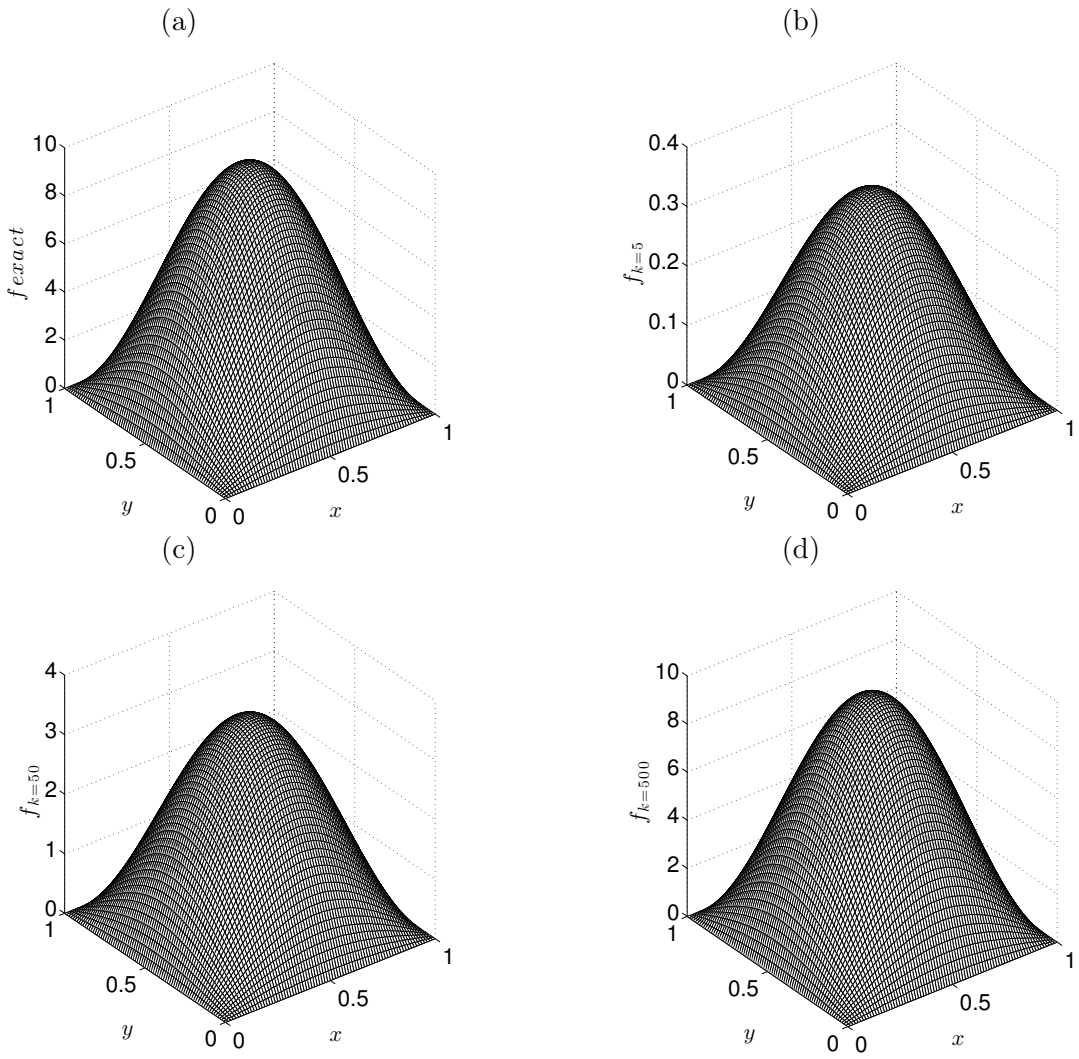

Figure 27: The numerical solution f_k for $k \in \{5, 50, 500\}$, in comparison with the exact solution (124), no noise for the inverse problem of Example 6.

In practice, the additional observation (126) comes from measurement which is inherently contaminated with errors. We therefore model this by replacing the exact data U_T by the noisy data

$$U_T^{\epsilon}(x_i, y_j) = U_T(x_i, y_j) + \epsilon_{i,j}, \quad i = \overline{1, (M-1)}, \quad j = \overline{1, (N-1)}, \tag{130}$$

where $(\epsilon_{i,j})_{i=\overline{1,M-1}, j=\overline{1,N-1}}$ are random noisy variables generated (using the MATLAB routine 'normrd') from a Gaussian normal distribution with mean zero and standard deviation $\sigma = p \times \max_{x,y\in[0,L]} |U_T(x, y)|$, where p represents the percentage of noise. The total amount of noise introduced in the cost functional (60) is then given by

$$\frac{1}{2}\epsilon^2 = \frac{1}{2}\sum_{i=1}^{M-1}\sum_{j=1}^{N-1}\epsilon_{i,j}^2. \tag{131}$$

In order to investigate the stability of the numerical solution we include some $p \in \{1, 3, 5\}\%$ noise into the input data (126), as given by equation (130). The objective function (128) and the accuracy error (129) are shown in Figures 28(a) and 28(b), respectively, for $k = \overline{1, 1000}$

and $p \in \{1, 3, 5\}\%$ noisy data. These figures yield the values of the stopping iteration numbers k_{discr} and k_{opt}, as given in Table 6.

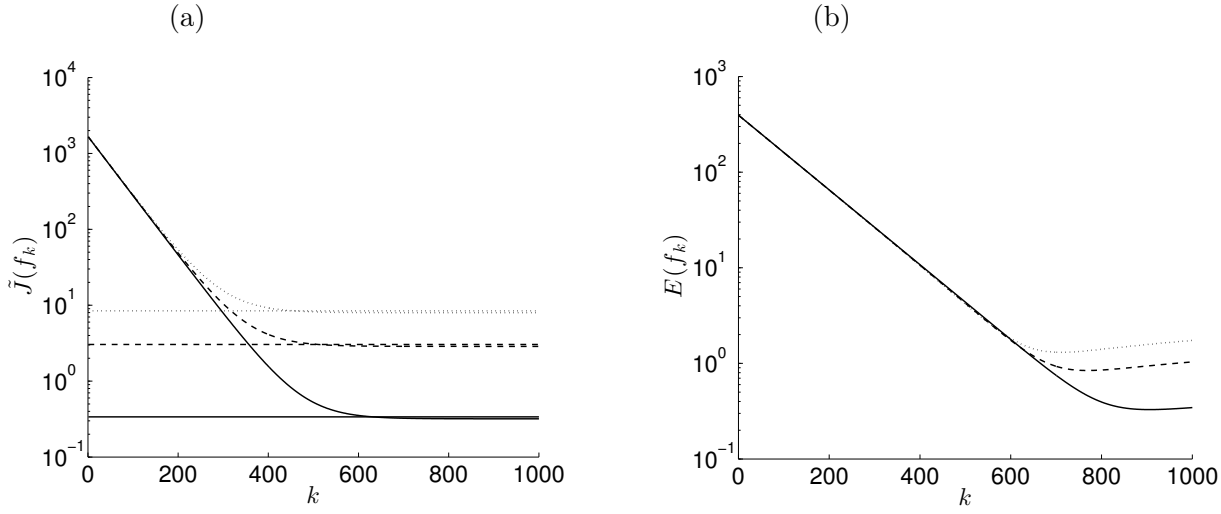

Figure 28: (a) The objective function (128) and (b) the accuracy error (129), versus the number of iterations $k = \overline{1, 1000}$, for $p = 1\%$ (—), $p = 3\%$ (- - -) and $p = 5\%$ ($\cdots$) noise for the inverse problem of Example 6. The horizontal lines represents the threshold $\tau^2 \frac{\epsilon^2}{2}$ with $\tau = 1.05$.

Table 6: The stopping iteration number k_{discr} chosen according to the discrepancy principle criterion (78) (with $\tau = 1.05$), as illustrated in Figure 28(a), and the optimal iteration number k_{opt} chosen according to the minimum of the accuracy error function (129) in Figure 28(b), for various percentages of noise $p \in \{1, 3, 5\}\%$ for Example 6. The corresponding accuracy errors $E(f_{k_{discr}})$ and $E(f_{k_{opt}})$ are also included.

p	1%	3%	5%
k_{opt}	906	769	711
$E(f_{kopt})$	0.3285	0.8425	1.3057
k_{discr}	796	599	597
$E(f_{kdiscr})$	0.4013	1.7573	1.8598

Finally, Figure 29 shows the analytical solution (124) for the force $f(x, y)$ in comparison with the numerical force $f_{k_{discr}}(x, y)$ for various percentages of noise $p \in \{1, 3, 5\}\%$. From this figure accurate and stable numerical predictions of the force can be observed.

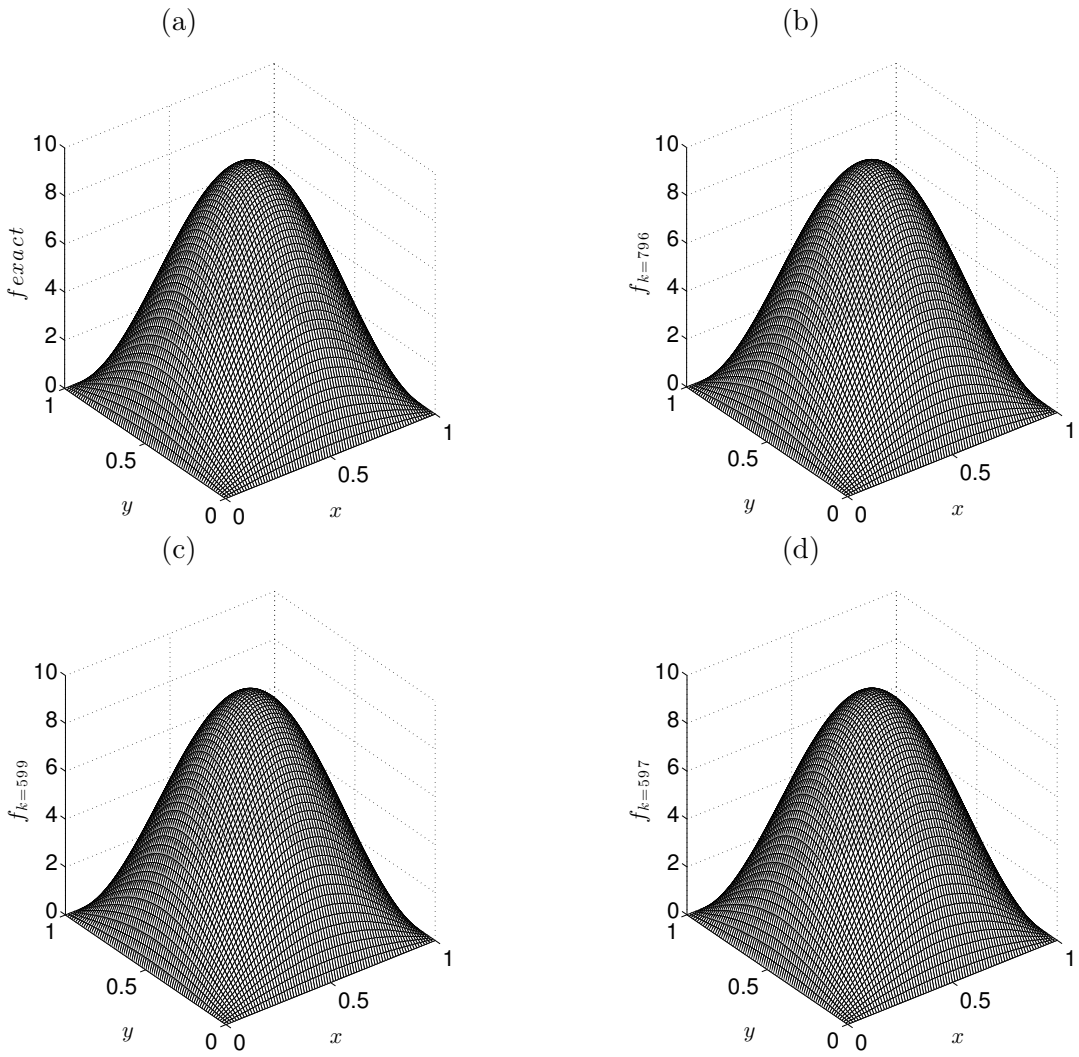

Figure 29: The exact solution (124) for f in comparison with the numerical solution f_k for $k_{discr} \in \{796, 599, 597\}$ for $p \in \{1, 3, 5\}\%$ noise, respectively, for the inverse problem of Example 6.

9 Conclusions

In this paper, the determination of the displacement and the space-dependent force acting on a vibrating structure from measured final or time-average displacement in the wave equation has been investigated. The linear inverse problems are uniquely solvable, but they are still ill-posed since small errors in the input data cause large errors in the output force. The problem has been discretised numerically using the FDM, and the Landweber method and CGM have been presented and discussed illustrating the convergence of the iterative procedures for exact input data and their stability for noisy data. Numerical results have been presented for both smooth and non-smooth examples. Furthermore, an extension to a two-dimensional example has also been illustrated in Section 8. Future work will consist in investigating the nonlinear inverse problem in which the unknown force depends on the displacement.

Acknowledgments

S.O. Hussein would like to thank the Human Capacity Development Programme (HCDP) in Kurdistan for their financial support in this research.

References

[1] Amirov, A. Kh. *On the question of solvability of inverse problems*, Soviet Mathematics Doklady, **34**, 258-259, 1987.

[2] Arendt, W., Batty, C.J.K., Hieber, M. and Neubrander, F. *Vector-valued Laplace Transforms and Cauchy Problems*, Springer, Basel AG, 2011.

[3] Cannon, J.R. and Dunninger, D.R. *Determination of an unknown forcing function in a hyperbolic equation from overspecified data*, Annali di Matematica Pura ed Applicata, **1**, 49-62, 1970.

[4] Chow, Y.T. and Zou, J. *A numerical method for reconstructing the coefficient in a wave equation*, Numerical Methods for Partial Differential Equations, DOI 10.1002/num.

[5] Elfving, T. and Nikazad, T. *Stopping rules for Landweber-type iteration*, Inverse Problems, **23**, 1417-1432, 2007.

[6] Engl, H.W., Scherzer, O. and Yamamoto, M. *Uniqueness and stable determination of forcing terms in linear partial differential equations with overspecified boundary data*, Inverse Problems, **10**, 1253-1276, 1994.

[7] Engl, H.W., Hanke, M. and Neubauer, A. *Regularization of Inverse Problems*, Kluwer Publ., Dordrecht, 2000.

[8] Erdem, A., Lesnic, D. and Hasanov, A. *Identification of a spacewise dependent heat source*, Applied Mathematical Modelling, **37**, 10231-10244, 2013.

[9] Hasanov, A. *Simultaneous determination of the source terms in a linear hyperbolic problem from the final overdetermination: weak solution approach*, IMA Journal of Applied Mathematics, **74**, 1-19.

[10] Hussein, S.O. and Lesnic, D. *Determination of a space-dependent source function in the one-dimensional wave equation*, Electronic Journal of Boundary Elements, **12**, 1-26, 2014.

[11] Hussein, S.O. and Lesnic, D. *Determination of forcing functions in the wave equation. Part I: the space-dependent case*, Journal of Engineering Mathematics, (accepted).

[12] Johansson, B.T. and Lesnic, D. *A variational method for identifying a spacewise-dependent heat source*, IMA Journal of Applied Mathematics, **72**, 748-760, 2007.

[13] Johansson, T. and Lesnic, D. *Determination of a spacewise dependent heat source*, Journal of Computational and Applied Mathematics, **209**, 66-80, 2007.

[14] Klibanov, M.V. *Inverse problems and Carleman estimates*, Inverse Problems, **8**, 575-596, 1992.

[15] Pilant, M.S. and Rundell, W. *Undetermined coefficient problems for quasilinear parabolic equations*, In: Inverse Problems in Partial Differential Equations, (eds. D. Colton, R. Ewing and W. Rundell), SIAM, Philadelphia, 165-185, 1990.

[16] Prilepko, A.I., Orlovsky, D.G. and Vasin, I.A. *Methods for Solving Inverse Problems in Mathematical Physics*, Marcel Dekker, Inc., New York, 2000.

[17] Slodicka, M. *Some uniqueness theorems for inverse spacewise dependent source problems in nonlinear PDEs*, Inverse Problems in Science and Engineering, **22**, 2-9, 2014.

[18] Yamamoto, M. *Stability, reconstruction formula and regularization for an inverse source hyperbolic problem by a control method*, Inverse Problems, **11**, 481-496, 1995.